Ridges, Seamounts, Troughs and Bowls: Topographic Control of the Dianeutral Circulation in the Abyssal Ocean

Journal of Physical Oceanography, 2018, 48 (4), 861-882

R. Holmes, C. de Lavergne and T.J. McDougall

Ridges, Seamounts, Troughs, and Bowls: Topographic Control of the Dianeutral Circulation in the Abyssal Ocean

RYAN M. HOLMES

School of Mathematics and Statistics, Climate Change Research Centre, and Australian Research Council Centre of Excellence for Climate System Science, University of New South Wales, Sydney, New South Wales, Australia

CASIMIR DE LAVERGNE AND TREVOR J. MCDOUGALL

School of Mathematics and Statistics, University of New South Wales, Sydney, New South Wales, Australia

(Manuscript received 14 July 2017, in final form 13 February 2018)

ABSTRACT

In situ observations obtained over the last several decades have shown that the intensity of turbulent mixing in the abyssal ocean is enhanced toward the seafloor. Consequently, a new paradigm has emerged whereby dianeutral downwelling dominates in the ocean interior and dianeutral upwelling only occurs within thin bottom boundary layers. This study shows that when mixing is bottom intensified the net abyssal dianeutral transports and the stratification can depend on subtle features of the seafloor geometry. Under an assumption of depth-independent net dianeutral upwelling, small changes in the curvature of the seafloor can result in interior stratification that is bottom intensified, uniform, or surface intensified. Further, when the net dianeutral transport is allowed to vary in the vertical, changes in the seafloor slope and bathymetric contour length with height can drive lateral exchange between the boundary layer and interior, with particularly strong lateral outflows predicted at the crests of midocean ridges. Finally, using a realistic neutral density climatology the authors suggest that the increase in the perimeter of abyssal neutral density surfaces with height drives much of the dianeutral upwelling at depths greater than 4 km, while the increase in the slope of the seafloor at shallower depths acts to oppose upwelling. These results add to a growing body of literature highlighting the key control of seafloor geometry on the abyssal overturning circulation.

1. Introduction

The turbulent mixing of buoyancy across neutral density surfaces in the ocean interior is thought to be a major control of both the vertical stratification and of the rate at which the deep ocean reservoirs of carbon and heat are renewed (Watson and Naveira Garabato 2006; Ferrari et al. 2014; Mashayek et al. 2015). Therefore, a major focus has been on understanding how, where, and how much the deep ocean mixes. The seminal study of Munk (1966) used a simple one-dimensional advection–diffusion balance to show that a vertical diffusivity of $10^{-4}\,\mathrm{m^2\,s^{-2}}$ was compatible with the observed Pacific deep hydrography. More recent discoveries, including the adiabatic upwelling of deep waters in the Southern Ocean (Toggweiler and Samuels 1995; Marshall and Speer 2012) and entrainment at depth into sinking bottom water plumes (Hughes and Griffiths 2006; Stewart et al. 2012), have called into question the need for such a strong diffusivity. Nevertheless, numerical simulations (Oka and Niwa 2013; Mashayek et al. 2015; Melet et al. 2016) and inverse models (Lumpkin and Speer 2007) suggest that the consumption of Antarctic Bottom Water (AABW) and the rate of overturning of the abyssal ocean, below 2000 m, depend strongly on both the magnitude and spatial structure of turbulent mixing.

Observations of turbulence in the abyssal ocean have shown that the turbulent kinetic energy dissipation rate ε is generally bottom intensified (Toole et al. 1994; Polzin et al. 1997; Ledwell et al. 2000; St. Laurent et al. 2012; Waterhouse et al. 2014; Sheen et al. 2014), owing to a number of processes including internal tide (St. Laurent and Garrett 2002; Garrett and Kunze 2007) and lee wave (Nikurashin and Ferrari 2011; Broadbridge et al. 2016) generation and breaking over rough topography, trapping of internal waves near the seafloor at

---

Corresponding author: Ryan M. Holmes, ryan.holmes@unsw.edu.au

DOI: 10.1175/JPO-D-17-0141.1

critical layers (Winters et al. 2011; Holmes et al. 2016), and strait mixing (Bryden and Nurser 2003). In turn this implies that the magnitude of the turbulent buoyancy flux per unit area $\mathcal{B}$ is also bottom intensified, where $\mathcal{B}$ is typically related to ε via $\mathcal{B} = \Gamma\varepsilon$ and the mixing efficiency Γ (Osborn 1980) is generally assumed constant in the interior (see section 2 for more discussion of this point). The bottom intensification of $\mathcal{B}$ has important consequences for the dianeutral velocity, or the fluid velocity crossing a neutral density surface, given for a linear equation of state (McDougall 1984) by

$$e = \frac{d\mathcal{B}}{db}, \tag{1}$$

where b is the buoyancy related, for example, to the neutral density of Jackett and McDougall (1997). Equation (1) implies that the dianeutral transport is downward, toward denser fluid, within the interior where $\mathcal{B}$ decreases with height. So how can mixing drive the upwelling necessary to balance the downwelling of dense waters? The solution to this apparent contradiction comes within the bottom boundary layers (BBLs). To satisfy the boundary condition at the seafloor, $\mathcal{B}$ must go to zero (or to the geothermal buoyancy flux) within the well-mixed BBL (Phillips 1970; Ledwell et al. 2000; Garrett 2001; Umlauf and Burchard 2011), and thus fluid parcels gain buoyancy there. If the seafloor is sloped, this gain in buoyancy drives an upwelling volume flux along the boundary at steady state. In the interior above the BBL, within what some authors have termed the "stratified mixing layer" (SML; Kunze et al. 2012; McDougall and Ferrari 2017), light waters are transformed into denser waters. This near-boundary circulation has been recognized in observations (Polzin et al. 1997; St. Laurent et al. 2001; Kunze et al. 2012).

The bottom intensification of mixing suggests that the geometry of the ocean's seafloor plays a controlling role in returning dense waters toward the surface (Wunsch 1970). The net dianeutral mass transport crossing a neutral density surface is given by the following (Walin 1982; Iudicone et al. 2008; Klocker and McDougall 2010):

$$\mathcal{E}_{\text{net}} = \frac{dF}{db}, \tag{2}$$

where

$$F(b) = \iint \mathcal{B}(x, y, b)\, dx\, dy, \tag{3}$$

is the buoyancy flux integrated over the same surface and we have ignored the geothermal heat flux. The density surface over which the area integration of Eq. (3) is performed lies in the ocean interior, and this density surface is not followed up to the sea surface inside the sinking plume of dense waters formed in the polar regions. Rather, the area integration is stopped at the outside edge of this sinking plume, such that $\mathcal{E}_{\text{net}}$ must be upward to balance the downward mass transport within the plume [as explained in McDougall and Ferrari (2017, their Fig. B1)]. According to Eq. (2) this requires that F increase with height (buoyancy). Because F depends closely on the area of a given neutral density surface that lies close to the seafloor where the mixing is strong (Klocker and McDougall 2010), whether or not this increase is achieved depends upon height changes of this mixing area. In turn, this area depends on several geometric factors, including the slope of topography, with a steeper slope implying a smaller area of a neutral density surface close to the bottom (Fig. 1a), and the total perimeter or circumference of a neutral density surface (Fig. 1b).

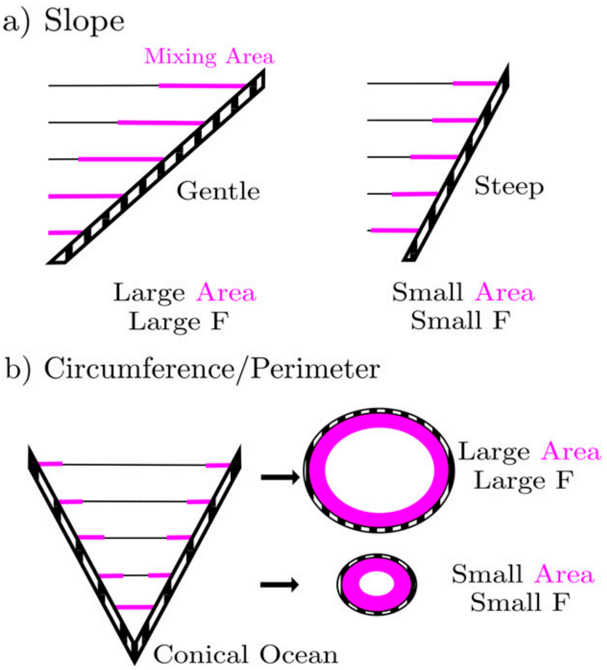

FIG. 1. Schematic demonstrating the two geometric factors that influence the area-integrated buoyancy flux F when mixing is bottom intensified. The vertical structure and peak magnitude of the local buoyancy flux are assumed not to vary, in order to isolate the role of topography. (a) Topographic slope: there is a larger near-bottom area on a given isopycnal where there is active mixing (magenta region) over a gentle slope compared to a steep slope, and therefore a larger area-integrated buoyancy flux F. (b) Topographic circumference: in a conical ocean with a constant slope there is a larger near-bottom area, and therefore F, at the top of the cone where the circumference is large compared to the base of the cone where the circumference is small.

A number of recent articles have begun to evaluate the importance of seafloor geometry for the abyssal overturning circulation. De Lavergne et al. (2016b,a) combine parameterizations for abyssal ocean sources of mixing with a climatological neutral density distribution to show that the transformation of AABW into lighter waters is strongly sensitive to the vertical structure of the buoyancy flux. This conclusion is supported by the global, energetically consistent numerical simulations of Melet et al. (2016). For a bottom-intensified buoyancy flux, de Lavergne et al. (2016b) show that the *incrop* area of neutral density layers into the topography exerts a strong control on the dianeutral circulation, with the peak incrop area at around 4000 m, or at a neutral density of ~28.11 kg m^{-3}, corresponding to a peak in net dianeutral upwelling. This idea was further developed by de Lavergne et al. (2017), who show that it is consistent with the observed distribution of abyssal radiocarbon and ocean ventilation patterns.

Ferrari et al. (2016) used a series of idealized numerical simulations to examine the influence of the vertical structure in the buoyancy flux and the role of sloping boundaries. They found that with bottom-intensified mixing a sloped seafloor produced a more realistic interior stratification than a flat seafloor. McDougall and Ferrari (2017) applied a buoyancy budget approach in density coordinates in the abyssal ocean to predict that up to 5 times as much volume is upwelled in the BBLs as is upwelled in the net. This "amplification factor" was obtained using a diagnostic relationship that assumed knowledge of the net dianeutral volume transport but did not explicitly include the dianeutral diffusive mixing processes that drive this transport. McDougall and Ferrari (2017) also discuss how these mixing processes are controlled by the seafloor geometry, and consider a number of idealized seafloor configurations, including two-dimensional oceans, conical seamounts, and conical oceans.

Many questions remain unanswered. The examples given in McDougall and Ferrari (2017) consider mostly constant slope geometries. When variations in, for example, slope are permitted, more complex features can emerge, such as the potential for lateral exchanges of fluid between the boundary layers and interior (Phillips et al. 1986; McDougall 1989; Garrett 1991; Visbeck and Rhein 2000; Kunze et al. 2012; Dell and Pratt 2015). Such vertical (or upslope) variations in the geometric, mixing, and stratification parameters were not considered in detail by the early boundary mixing papers of Wunsch (1970), Phillips (1970), Thorpe (1987), Garrett (1990), and others.

In this article we seek to build on these previous studies, asking the following questions: 1) What aspects of the topography influence the dianeutral circulation? McDougall and Ferrari (2017) suggested that the vertical structure in both slope and perimeter play a role, but did not elaborate. 2) How does topography influence the interior stratification? 3) What dianeutral circulations should we expect around major topographic features such as seamounts and midocean ridges?

We address these questions by considering some simple geometries and examining the relationship between the net dianeutral transport $\mathcal{E}_{\mathrm{net}}$, the area-integrated buoyancy flux F and the stratification db/dz implied by Eq. (2). That is, we will specify two of these parameters and solve for the third. We will not consider the momentum budget, and to make the system analytically tractable we will assume that neutral density surfaces are flat in the interior. Furthermore, in order to isolate the role of topography we will assume a simple vertical structure for the diffusive buoyancy flux and assume that its peak magnitude is uniform laterally. This idealized, process-oriented approach contrasts with box inverse methods (e.g., Ganachaud and Wunsch 2000) in that mixing is specified rather than inferred, yielding different yet complementary information about stratification, circulation, and their relationship to topography.

Given the simple system captured by Eq. (2) and a specified bottom-intensified buoyancy flux, we will show that subtle changes in the curvature of topography can have important implications for the abyssal stratification (section 3) and dianeutral circulation (section 4). We compare results using these bottom-intensified buoyancy fluxes to those obtained if the buoyancy fluxes are constant with height (implying dianeutral transport only in the BBL) or if the vertical diffusivity is constant (as considered by Munk 1966). We then apply some of these ideas to the Mid-Atlantic Ridge (MAR) and a section of the South Pacific (SP), examining how the topography in these regions may influence the dianeutral circulation in their vicinity (section 5). Finally, for the global ocean we decompose the vertical variations in the incrop area into averaged variations of the seafloor slope and the perimeter of neutral density surfaces, suggesting that it is an increase in the perimeter of neutral density surfaces (rather than changes in slope) that drives much of the upwelling of dense waters in the abyss (section 6).

2. Analytical framework

We begin by describing the theoretical framework on which the rest of the article is based. We will look for a steady-state dianeutral circulation where the interior buoyancy b varies only with height z. This is a reasonable approximation at regional scales in the abyssal ocean, and the results can be generalized to curved neutral density surfaces if the topographic slopes and areas are reinterpreted in buoyancy space. For example, a flat bottom underneath a sloping neutral density surface corresponds to a sloped bottom in buoyancy space, termed *pseudohypsometry* by de Lavergne et al. (2016b).

Following McDougall and Ferrari (2017), we consider a bottom-intensified buoyancy flux per unit area $\mathcal{B}(x, y, z)$ with the following form (Fig. 2):

$$\mathcal{B}(x,y,z) = \mathcal{B}_0[z - h(x,y)]/h_{\mathrm{BBL}}, \quad z - h(x,y) < h_{\mathrm{BBL}}, \tag{4}$$

and

$$\mathcal{B}(x,y,z) = \mathcal{B}_0 \exp\{-[z - h(x,y) - h_{\mathrm{BBL}}]/d\}, \quad z - h(x,y) > h_{\mathrm{BBL}}. \tag{5}$$

The buoyancy flux per unit area $\mathcal{B}$ increases linearly from zero at the bottom boundary [$z = h(x, y)$, where $h(x, y)$ is the ocean depth] to $\mathcal{B}_0$ at the top of a BBL of thickness h_{BBL} [note that z is zero at the sea surface and $h(x, y)$ is negative]. Above the BBL $\mathcal{B}$ decreases exponentially with a scale height d (Fig. 2), in approximate correspondence with available in situ observations (St. Laurent et al. 2002; Kunze 2017; Waterhouse et al. 2014). As discussed by McDougall and Ferrari (2017), this choice of an exponential is one of analytical convenience, and a different choice of structure, providing it decays in the vertical, will yield similar qualitative results.

Our choice of vertical structure for $\mathcal{B}$ is based on observations of the turbulent kinetic energy dissipation rate ε and an assumption of a weakly varying mixing efficiency Γ. While the mixing efficiency is known to vary in the interior deep ocean (Ivey et al. 2008; Mashayek et al. 2017; Gregg et al. 2018), these variations in Γ are unlikely to override the vertical decay of $\mathcal{B}$ in the interior and therefore qualitatively alter our results. Quantitatively, of course, variations in the mixing efficiency may play a role by altering the decay scale d or the peak buoyancy flux magnitude $\mathcal{B}_0$ (de Lavergne et al. 2016a; Mashayek et al. 2017).

Throughout this article we will consider $\mathcal{B}_0$ to be laterally uniform. While this is a gross simplification, as for example mixing is observed to be stronger over regions of rough topography (Waterhouse et al. 2014), it allows us to isolate the role of seafloor geometry. McDougall and Ferrari (2017) considered four factors that could drive the net upwelling of dense waters [their Eq. (34)]. These factors were changes with buoyancy of 1) $\mathcal{B}_0$, 2) the topographic slope, 3) the topographic circumference, and 4) the vertical decay scale d. In this article we focus on the geometrical factors 2 and 3.

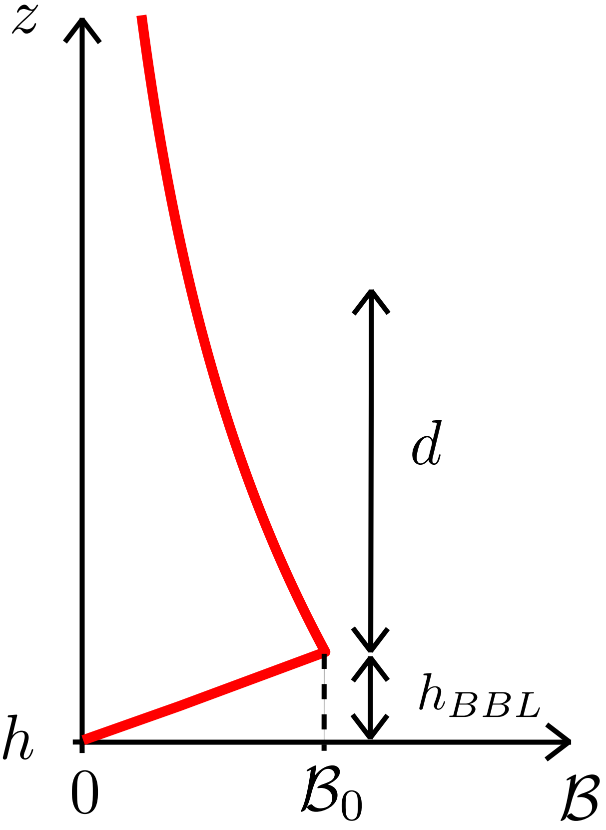

FIG. 2. The vertical structure of the turbulent buoyancy flux per unit area $\mathcal{B}$ used in this article as a function of height above bottom. The $\mathcal{B}$ increases linearly to a maximum value of $\mathcal{B}_0$ at the top of the BBL of height h_{BBL} and then decreases exponentially with scale height d.

The diffusive buoyancy flux per unit area $\mathcal{B}$ drives a net (area integrated) vertical dianeutral transport $\mathcal{E}_{\mathrm{net}}$, related to the magnitude of the area-integrated buoyancy flux $F(b)$ [Eq. (3)] through Eq. (2). The relation in Eq. (2) can be achieved through different configurations of topography and interior stratification providing that

$$\frac{dF}{dz} = \mathcal{E}_{\mathrm{net}}(z)\frac{db}{dz}. \tag{6}$$

Equation (6) constrains $F(z)$ given upwelling and stratification profiles. However, underlying $F(z)$ here is the topography, allowing us to make the counterintuitive step of solving Eq. (6) for the topography from upwelling and stratification profiles (section 3). We will see that such an approach yields a number of important insights that would not be obtained if the topography was completely specified a priori.

To solve Eq. (6) for the topography, we first make some broad assumptions about the form of that topography. We will consider a number of idealized topographic configurations (Fig. 3): a two-dimensional *trough* or *ridge*, where the topography is uniform in the Cartesian x direction with vertical sides at the two ends, and a three-dimensional circular *bowl* or *seamount*, where the topography is uniform in the azimuthal x direction and specified as a function of the radius y. For the 2D trough and ridge the circumference is constant [$L(y) = L_c$], while for the 3D

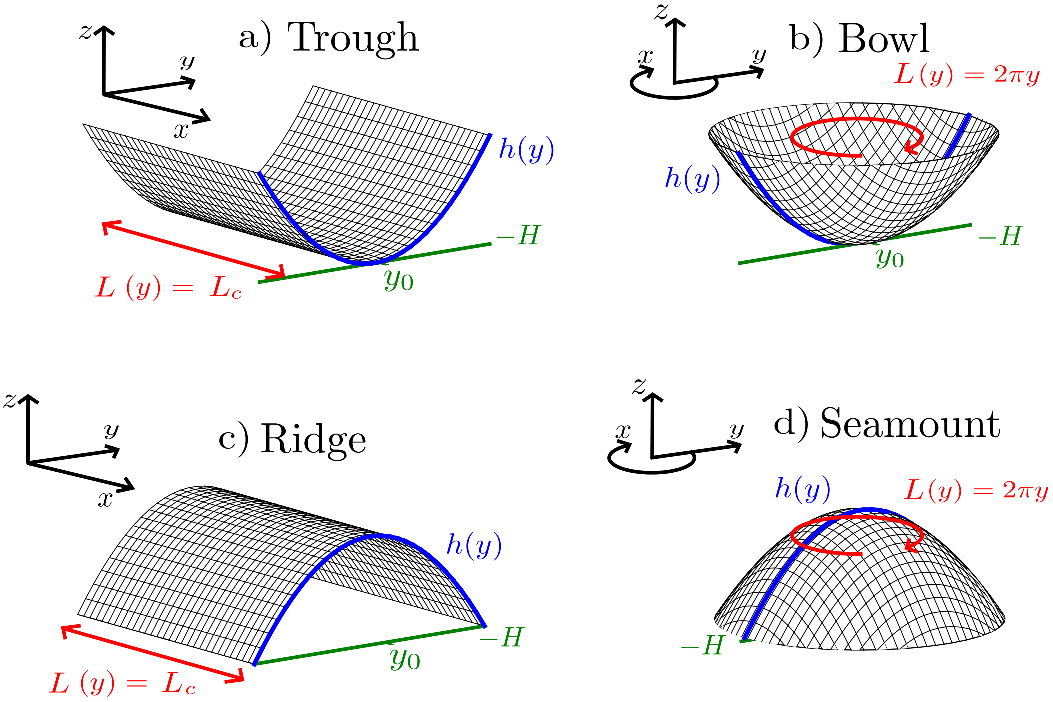

FIG. 3. Schematics of the four simplified geometries considered in this article. They differ by whether the topography shoals (trough, bowl) or deepens (ridge, seamount) away from y_0 and whether the symmetry is Cartesian (trough, ridge), where the circumference $L(y)$ is constant, or circular (bowl, seamount), where the circumference $L(y)$ increases linearly with y.

bowl and seamount, the circumference changes linearly with y [$L(y) = 2\pi y$].

Given the above assumptions we solve Eq. (6) for the topography (see appendix A for details):

$$\mathcal{B}_0 L \frac{dr}{dz} = \frac{dF}{dz} + \frac{F}{d}, \qquad (7)$$

where dr/dz is the inverse topographic slope and $F(z)$ on the RHS is known through an integral of Eq. (6),

$$F(z) = \int_{-H+h_{\mathrm{BBL}}}^{z} \frac{db}{dz} \mathcal{E}_{\mathrm{net}}\, dz\,. \qquad (8)$$

The topographic radius $r(z)$, the inverse function of $z = h(y) + h_{\mathrm{BBL}}$, can then be obtained from Eq. (7) via an integral and finally inverted to obtain $h(y)$.

Equation (7) is the key equation of this article, and there are several features that are worth highlighting. First, this equation becomes singular when the topography is flat where the inverse slope $dr/dz \to \infty$. In this case our flat interior neutral density surfaces are parallel to the boundary and there can be no along-boundary dianeutral advection to balance the near-bottom convergence of the diffusive buoyancy flux (Mashayek et al. 2015). In this situation a stratified steady state is not possible and the geometry of the neutral density surfaces would change, as observed in the flat-bottom simulations of Ferrari et al. (2016).

Second, the LHS of Eq. (7) is proportional to the vertical derivative of the total area of our simple ocean basin:

$$\frac{dA}{dz} = L \frac{dr}{dz}, \qquad (9)$$

where

$$A = \int_{y_0}^{r(z)} L(y)\, dy\,. \qquad (10)$$

The area derivative dA/dz is related to both the incrop area of de Lavergne et al. (2016b), given by dA/db, and the area within the SML, A_{mix}, discussed by McDougall and Ferrari (2017) (see appendix A) and shown by the magenta regions in Fig. 1. Equations (7) and (8) provide us with a simple relationship between seafloor geometry, the stratification, and dianeutral upwelling. In fact, under the limit of weak vertical variations in the slope and circumference (with respect to d such that $d/dz \ll 1/d$; see appendix A), dF/dz is small relative to F/d in Eq. (7), and we find that

$$F(z) \approx \mathcal{B}_0 d \frac{dA}{dz} \approx \mathcal{B}_0 A_{\text{mix}}, \tag{11}$$

indicating that F is simply proportional to the area of active mixing in the SML A_{mix}, as intuition (and Fig. 1) suggests.

3. Uniform net dianeutral upwelling

We now examine the relationship between the stratification of the ocean interior and the topography under the assumption of a depth-independent net dianeutral upwelling $\mathcal{E}_{\text{net}}(z) = \mathcal{E}_{\text{net}}$. This is equivalent to assuming that there is no entrainment or detrainment into the descending dense bottom water plume, so that, effectively, the source of bottom water can be regarded as entering at the bottom of the ocean through an impervious pipe. This case was considered in Rhines and MacCready (1989) and McDougall and Ferrari (2017).

We examine an interior stratification with the following form:

$$\frac{db}{dz} = N_0^2 e^{(z+H-h_{\text{BBL}})/s}, \tag{12}$$

allowing us to consider three possibilities: exponentially increasing ($s > 0$), decreasing ($s < 0$), and constant ($s \to \infty$) stratification. Given this stratification and the assumption of depth-independent net dianeutral upwelling, we can obtain formulas for the topographic slope of the trough, bowl, ridge, and seamount geometries required for a consistent solution (see appendix A). For plotting purposes we make the specific parameter choices $d = 500\,\text{m}$, $h_{\text{BBL}} = 100\,\text{m}$, $\mathcal{E}_{\text{net}} = 10\,\text{Sv}$ ($1\,\text{Sv} \equiv 10^6\,\text{m}^3\,\text{s}^{-1}$), $\mathcal{B}_0 = 5 \times 10^{-9}\,\text{m}^2\,\text{s}^{-3}$, and $H = 5000\,\text{m}$. The constant N_0^2 is chosen to yield a stratification of $10^{-6}\,\text{s}^{-2}$ at a depth of 3000 m, with a scale height $s = 1500\,\text{m}$ for the nonconstant cases. The value of $\mathcal{B}_0$ is chosen such that the topography $h(y)$ rises from 5000 to ~1000 m over a lateral distance of ~4000 km. The length of the 2D domain L_c is chosen so that the radial extent approximately matches that of the circular domain. Qualitative conclusions, discussed below, do not depend on the specific parameter choices made.

a. The trough and bowl

We first consider the trough and bowl geometries. We find that the trough topography has a negative curvature for all three stratifications, such that the slope always decreases with height (or the inverse slope dr/dz always increases with height; Figs. 4c,i,o). The circumference is constant in this 2D geometry, meaning that this negative curvature is the only way in which the area of an isopycnal near the boundary (the SML area A_{mix}; magenta line in Figs. 4b,h,n), and therefore the area-integrated buoyancy flux F, can increase with height to permit net upwelling $dF/db > 0$.

The stratification does however influence the magnitude of the slope curvature. Given constant upwelling, larger stratification requires larger buoyancy gain dF/dz. Thus when the stratification increases with height (top row in Fig. 4), the change in slope with height is more rapid. In contrast, when the stratification decreases with height (bottom row in Fig. 4) the curvature need not be strong, and, in fact, the slope asymptotes to a constant as the stratification becomes weak. For constant stratification the slope decreases linearly (solid line in Fig. 4i) to match the linearly increasing F (black line in Fig. 4h).

For the bowl geometry the circumference is not constant, and thus A_{mix} can vary with height even if the slope is constant (Fig. 1b). Consequently, the bowl requires less negative slope curvature than the trough to support the same upwelling and stratification. For the exponentially increasing stratification (Fig. 4e), the slope curvature must still be negative as for the trough. However, for constant stratification, the bowl slope is constant (once above the base of the bowl; dashed line in Fig. 4i) because the linear increase in F can be achieved simply through the linear dependence of the bowl's circumference on radius and height. For the exponentially decreasing stratification (Fig. 4q), the bowl must be positively curved in order to counteract the increase in circumference with height.

Note that these trends are not strictly followed near the deepest part of the domain. Here, there is a nonzero buoyancy flux at all lateral locations y, and thus A_{mix} is equal to the total area of the basin (neglecting the small area within the BBL) instead of being proportional to its height derivative [Eq. (A3)]. This important effect will be discussed in more detail in section 5.

b. The ridge and seamount

Similar geometric constraints apply to the ridge and seamount geometries (Figs. 3c,d). In fact, the ridge slope is identical to the trough, other than being of the opposite sign (Figs. 5d,j,p). Therefore, as before, the slope always decreases to allow an increase in A_{mix} with height, culminating in a sharp ridge crest. However, the seamount slope differs significantly from the bowl (cf. dashed lines in Figs. 5c,i,o to Figs. 4c,i,o). To sustain upwelling up to its crest, the seamount must be negatively curved for all three stratifications in order to compensate for the reduction in its circumference. The reduction in the circumference of a seamount approaching its crest generally acts to reduce the area of mixing toward the top of the seamount, suggesting that a net downwelling of fluid should surround the seamount flanks, as discussed by McDougall (1989) and McDougall and Ferrari (2017). However, McDougall (1989) took the radial width of the

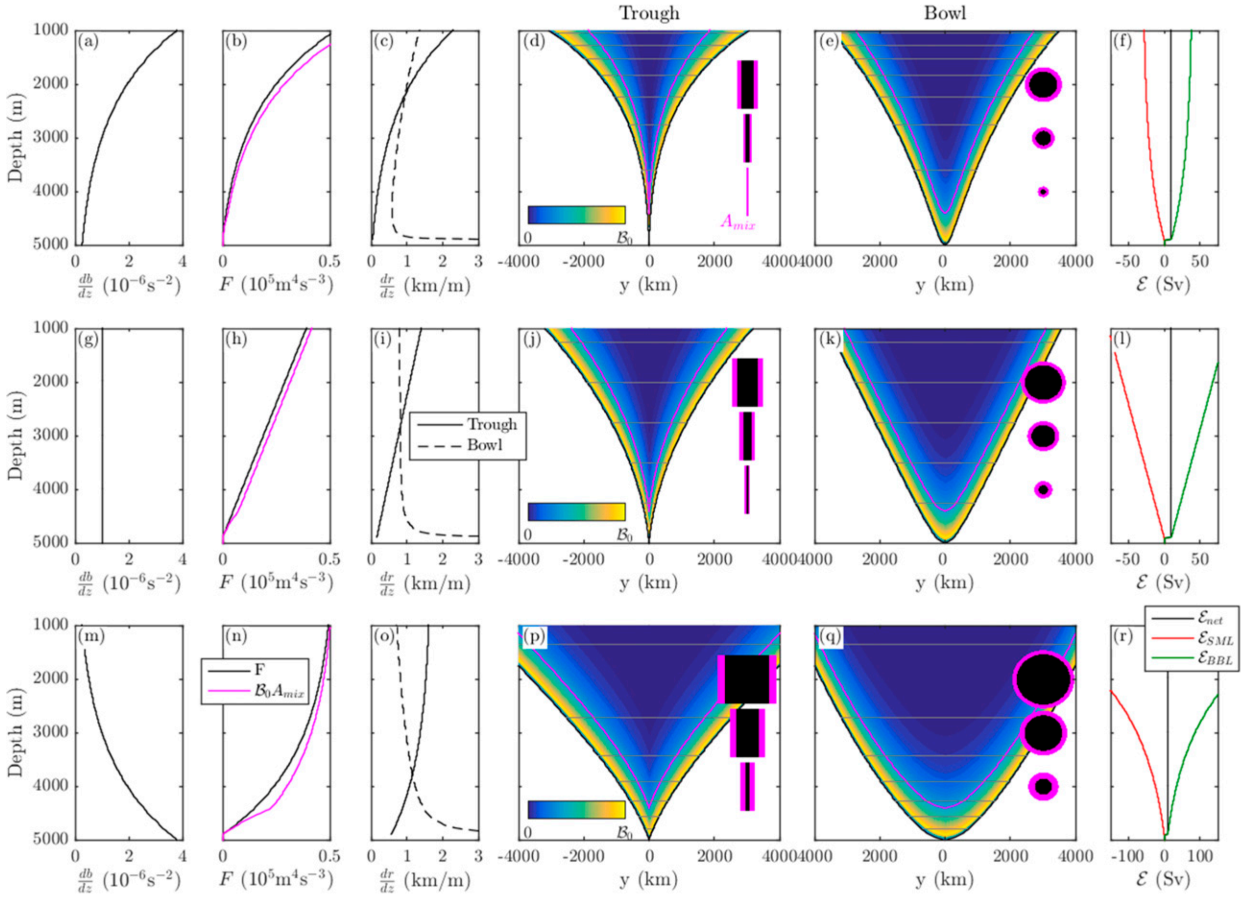

FIG. 4. Solutions for the trough and bowl geometries given constant net dianeutral upwelling $\mathcal{E}_{\rm net} = 10$ Sv and (top),(a)–(f) exponentially increasing, (middle),(g)–(l) constant, and (bottom),(m)–(r) exponentially decreasing (a),(g),(m) stratification db/dz. The area-integrated buoyancy flux F and (b),(h),(n) area of the SML $A_{\rm mix}$, (c),(i),(o) the inverse slope of topography, (d),(j),(p) the trough with buoyancy flux, (e),(k),(q) the bowl with buoyancy flux, and (f),(l),(r) the dianeutral transports. The inset panels in (d), (e), (j), (k), (p), and (q) represent top-down views of the domain at 2000, 3000 and 4000 m, with magenta indicating the area of the SML and black indicating weak mixing within the domain. The gray lines in (d), (e), (j), (k), (p), and (q) are neutral density surfaces, and the magenta line indicates the height one e-folding distance above the BBL.

annular area of the mixing region surrounding a seamount to be independent of height, while McDougall and Ferrari (2017) treated only a conical seamount of fixed slope at all heights. The examples we have discussed here overcome these past unrealistic assumptions, showing that it is possible to get upwelling below the crest of a seamount providing that the reduction in the slope with height dominates the reduction in the circumference. Note that above the crests of both the ridge and seamount, upwelling is not possible as F decreases with height (see section 4).

c. The amplification factor

We now discuss the behavior of the dianeutral transports in the BBL, SML, and the net (Figs. 4f,l,r and 5f,l,r). The net dianeutral transport in the SML is given by the following [obtained from Eqs. (5) and (A1)]:

$$\mathcal{E}_{\rm SML} \equiv \int \frac{d\mathcal{B}}{db}\,dA = -\frac{F}{d}\left(\frac{db}{dz}\right)^{-1}. \qquad (13)$$

The net transport in the BBL is then given by the difference:

$$\mathcal{E}_{\rm BBL} = \mathcal{E}_{\rm net} - \mathcal{E}_{\rm SML}. \qquad (14)$$

Equation (13) reveals that our key Eq. (7), when multiplied by the inverse stratification, is simply equivalent to Eq. (14), the dianeutral flux identity between the BBL transport [associated with changes in the area of the basin dA/dz; LHS of Eq. (7)], the net transport [associated with dF/dz in Eq. (7)], and the SML transport [associated with F/d in Eq. (7)]. Note that these transports do not depend on the specific geometry chosen, only on F and db/dz. This is also true for the amplification factor (McDougall and Ferrari 2017):

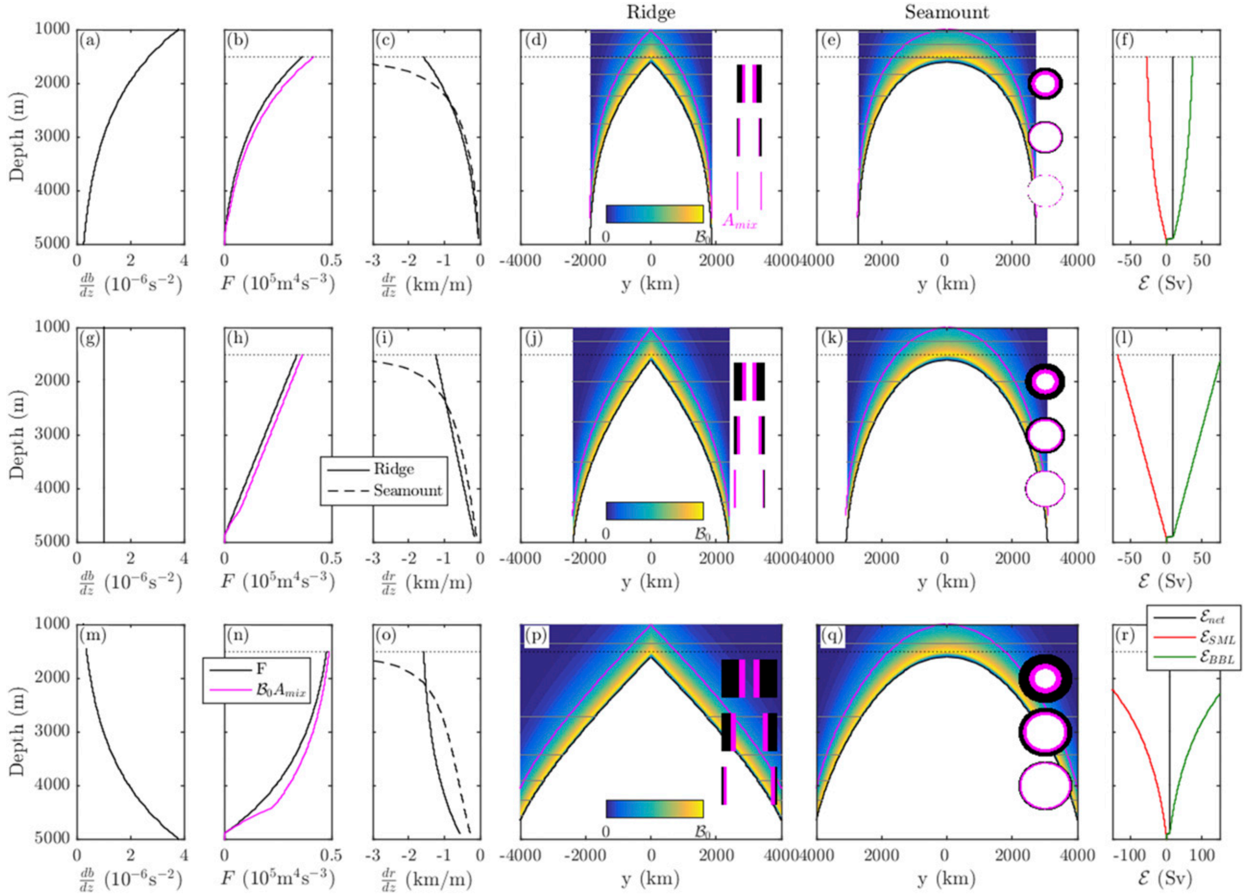

FIG. 5. As in Fig. 4, but for the (d),(j),(p) ridge and (e),(k),(q) seamount geometries. Note that above the crest of the topography (horizontal dotted lines) it is not possible to have net upwelling and thus F, dr/dz, and the dianeutral transports are not shown there.

$$\mathcal{A} \equiv \frac{\mathcal{E}_{\text{BBL}}}{\mathcal{E}_{\text{net}}} = 1 + \frac{|\mathcal{E}_{\text{SML}}|}{\mathcal{E}_{\text{net}}} = 1 + \frac{1}{\mathcal{E}_{\text{net}} d}\left(\frac{db}{dz}\right)^{-1}\int_{b_{\text{min}}}^{b}\mathcal{E}_{\text{net}}\,db', \tag{15}$$

where the last step [obtained by integrating Eq. (2) and substituting into Eq. (13)] is the key diagnostic equation of McDougall and Ferrari (2017), illustrating how $\mathcal{A}$ can be obtained with knowledge only of $\mathcal{E}_{\text{net}}(b)$, db/dz, and the buoyancy flux decay-scale d.

For constant net upwelling (i.e., $\mathcal{E}_{\text{net}}$ being independent of buoyancy) the three different stratifications considered above yield SML transports [combining Eqs. (13) and (12)]:

$$\mathcal{E}_{\text{SML}} = -\frac{s}{d}\mathcal{E}_{\text{net}}[1 - e^{-(z+H-h_{\text{BBL}})/s}], \quad \text{exponential } db/dz, \tag{16}$$

and

$$\mathcal{E}_{\text{SML}} = -\frac{1}{d}\mathcal{E}_{\text{net}}(h_{\text{BBL}} - z - H), \quad \text{constant } db/dz. \tag{17}$$

For the most realistic case of exponentially increasing stratification [Eq. (16) with $s > 0$], when more than one or two e-folding depths above the basin bottom, there is constant downwelling in the SML, constant upwelling in the BBL, and a constant amplification factor (Figs. 4f and 5f):

$$\mathcal{A} = 1 + \frac{s}{d}. \tag{18}$$

The limiting value of the amplification factor is determined simply by the ratio of the vertical e-folding scales of buoyancy s, and of the mixing intensity $\mathcal{B}$, d. This simple relationship is a consequence of the dependencies of $\mathcal{E}_{\text{net}}$ and $\mathcal{E}_{\text{SML}}$ on F, which is then eliminated in their ratio. In our case s = 1500 m and d = 500 m, so $\mathcal{A}$ asymptotes to 4. McDougall and Ferrari (2017) estimated an amplification factor that increased from 1 at the bottom to 5 at 2500 m based on Eq. (15) and the large-scale net upwelling structure $\mathcal{E}_{\text{net}}(b)$ estimated by Lumpkin and Speer (2007).

For constant stratification, $\mathcal{E}_{\text{SML}}$ and $\mathcal{A}$ both increase linearly with height (Figs. 4l and 5l). Under the

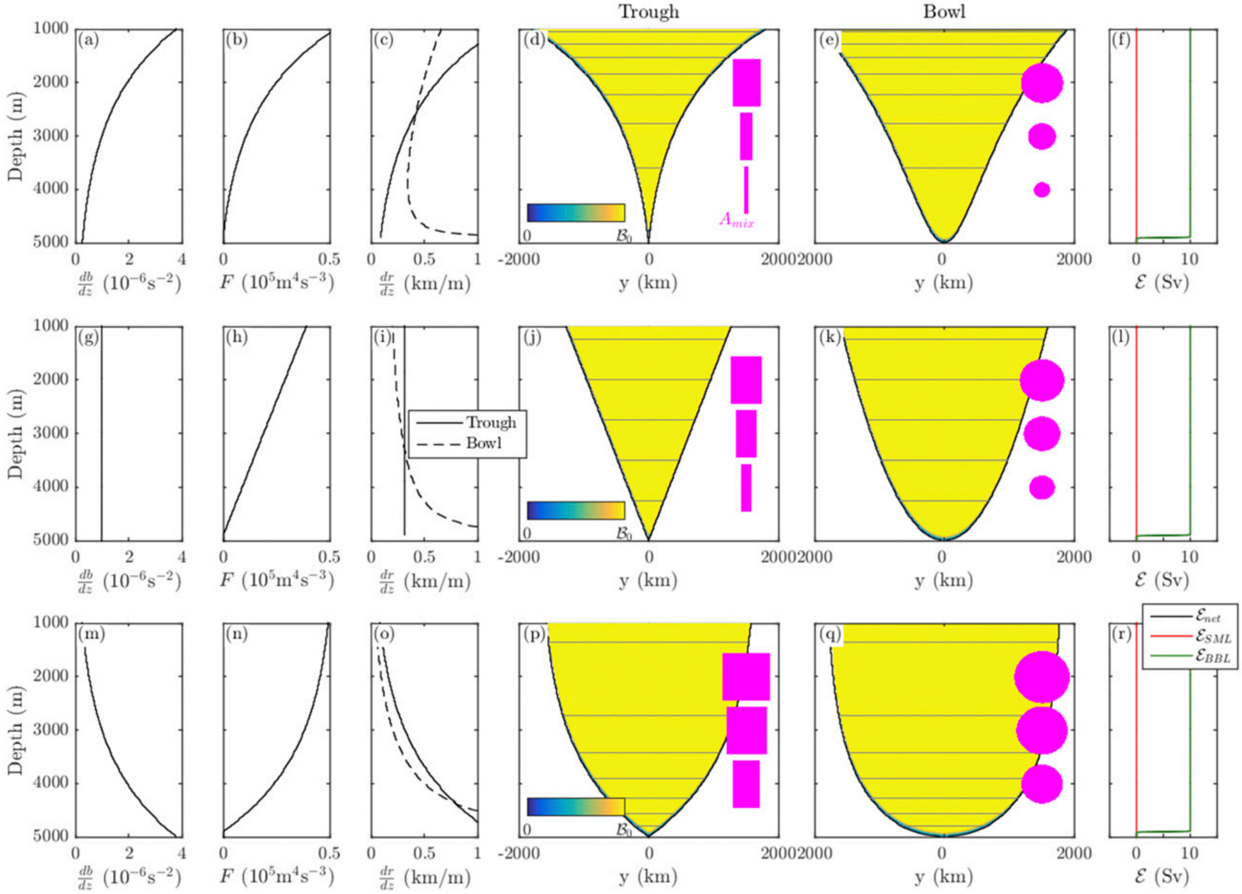

FIG. 6. As in Fig. 4, but for the limit that $d \to \infty$, where the buoyancy flux per unit area is constant, $\mathcal{B} = \mathcal{B}_0$, in the interior.

exponentially decreasing stratification, $\mathcal{E}_{\mathrm{SML}}$ and $\mathcal{A}$ increase exponentially with height (Figs. 4r and 5r). In this case $\mathcal{A}$ can become very large, with transports in the SML and BBL reaching over 150 Sv above 2000 m for the same net upwelling of 10 Sv. This is because $\mathcal{E}_{\mathrm{SML}}$ increases in proportion to F and must be large in weakly stratified regions to balance the mixing-driven buoyancy tendency [Eq. (13)].

d. A uniform buoyancy flux

One interesting limit to consider is $d \to \infty$, where the buoyancy flux per unit area is constant in the interior. Note that this also captures the water-mass transformation driven by a horizontally uniform geothermal heat flux at the seafloor. A geothermal flux drives a lightening of fluid only in the BBL and thus produces the same dianeutral mass flux as a uniform buoyancy flux, which decays only in the BBL (Emile-Geay and Madec 2009; de Lavergne et al. 2017).

The area-integrated buoyancy flux F in this case is simply equal to the total area of fluid outside the BBL times $\mathcal{B}_0$ (Fig. 6), and the last term in Eq. (7), F/d, drops out. This is fundamentally different from the bottom-intensified case, where F/d dominated over dF/dz, as there is now one additional height derivative between the inverse slope dr/dz and F.

Consequently, it is no longer necessary that the slope of the 2D trough be negatively curved in order to support upwelling (Figs. 6d,j,p). Instead we only require a nonzero slope as this will always drive an increase in total area (i.e., hypsometry; Rhines and MacCready 1989). This is also true for the bowl, with the additional increase in the circumference accounting for the differences compared to the trough (Figs. 6e,k,q).

We also note that with a uniform buoyancy flux per unit area, all of the upwelling is achieved in the BBL and there is no dianeutral transport in the interior (Figs. 6f,l,r). We do not consider the ridge or seamount cases for $d \to \infty$ because the mixing is no longer localized close to the topographic feature and remote effects become important.

e. Constant diffusivity

Finally, we can also consider the case of a constant diffusivity κ, following Munk (1966). With a constant diffusivity and a stratification only dependent on height, the buoyancy flux per unit area in the interior is now a function of height only, as opposed to height above bottom. Thus, the area-integrated buoyancy flux F is simply

$$F(z) = \kappa \frac{db}{dz} A(z). \tag{19}$$

Combining this with Eq. (6), we can obtain a simple equation for the net dianeutral upwelling:

$$\mathcal{E}_{\mathrm{net}} = \kappa \frac{dA}{dz} + \kappa A \left(\frac{db}{dz}\right)^{-1} \frac{d}{dz}\left(\frac{db}{dz}\right). \tag{20}$$

The second term here is easily identified as $\mathcal{E}_{\mathrm{SML}}$ [substitute $\mathcal{B} = \kappa(db/dz)$ in the integral of Eq. (13)]. Using only the second term in Eq. (20), and dividing by A, we obtain the one-dimensional balance equation,

$$\frac{\mathcal{E}_{\mathrm{net}}}{A} = \kappa \left(\frac{db}{dz}\right)^{-1} \frac{d^2 b}{dz^2}, \tag{21}$$

used by Munk (1966) to obtain the value $\kappa_M = 10^{-4}\,\mathrm{m^2\,s^{-1}}$ consistent with a set of observed temperature, salinity, and radiocarbon profiles from the abyssal Pacific. However, this local interior balance excludes the first term in Eq. (20) associated with the hypsometry of the abyssal ocean and with flow in the BBL:

$$\mathcal{E}_{\mathrm{BBL}} = \kappa \frac{dA}{dz}. \tag{22}$$

This term may become large where basin areas shrink rapidly with depth, as occurs below about 3000 m in the main basins of the World Ocean (see section 6).

As above, we can again solve for the topography. For the most realistic case of exponentially increasing stratification, combining Eq. (19) with Eqs. (A4) and (A5) for F yields

$$A(z) = \frac{s\mathcal{E}_{\mathrm{net}}}{\kappa}\left[1 - e^{-(z+H-h_{\mathrm{BBL}})/s}\right]. \tag{23}$$

The trough and bowl topographies are then obtained simply through $r(z) = A(z)/L_c$ and $r(z) = \sqrt{A(z)/\pi}$, respectively. For both the trough and bowl we see a continual increase in the sidewall slope with height (Fig. 7). Sufficiently far above the bottom the area of the basin approaches a constant, the sidewalls become vertical, and the BBL transport vanishes (green line in Fig. 7f). Given increasing stratification the buoyancy flux per unit area due to a constant diffusivity is everywhere increasing with height, and so upwelling can be supported through the interior ($\mathcal{E}_{\mathrm{SML}}$ is positive; red line in Fig. 7f) without a BBL transport. This is fundamentally different from the bottom-intensified mixing case, hypsometry playing a much weaker role here.

4. Lateral exchange between the boundary layers and the interior

We now relax the assumption of vertically uniform net dianeutral upwelling and instead specify the topography and stratification, solving for the dianeutral transport. In general, the resulting net dianeutral transport will have convergences and divergences, which in a steady state implies the existence of inflows and outflows along neutral density surfaces to and from the topographic feature of interest. Without an entraining or detraining plume within the domain, such inflows and outflows are not possible within the bowl and trough geometries. Thus we consider only the ridge and seamount and assume that there are far-field processes that maintain a fixed stratification in the interior.

We examine a parabolic ridge or seamount defined by

$$h(y) = z_0 - \frac{y^2}{a^2}, \tag{24}$$

where z_0 is the height of the crest and a measures the width of the feature. We then obtain the area-integrated buoyancy flux F by applying the exponential vertical structure for the buoyancy flux per unit area [Eqs. (4) and (5)] and integrating at constant height (see appendix A).

There are clear differences in F between the ridge and seamount below their crests (cf. dashed and solid lines in Fig. 8c). For the ridge, F increases exponentially with height approaching from below the flat crest where A_{mix} is large. This is unlike the ridges in the previous section, whose crests were sharp (cf. Fig. 8b to Figs. 5d,j,p). However, below the crest of the seamount F is constant as the reduction in circumference with height exactly balances the effect of the reduction in slope (as the change in area of a paraboloid with height is constant). The same balance between the effects of circumference and slope was noted by McDougall and Ferrari (2017) at the bottom of a spherical bowl ocean. Above the crests of both the ridge and the seamount F decays exponentially.

These forms for F have interesting implications for the net dianeutral transport $\mathcal{E}_{\mathrm{net}}$ (Figs. 8e,f). As discussed by McDougall (1989), $\mathcal{E}_{\mathrm{net}}$ is downward above both the ridge and seamount and decreases with height. This implies that both the seamount and ridge are lateral sinks of fluid above their crests, as $\mathcal{E}_{\mathrm{net}}$ diverges there (Fig. 8g).

In contrast, below the crest of the seamount $\mathcal{E}_{\mathrm{net}}$ is zero (black line in Fig. 8f), as F is constant. This implies that there is a large lateral outflow into the interior right

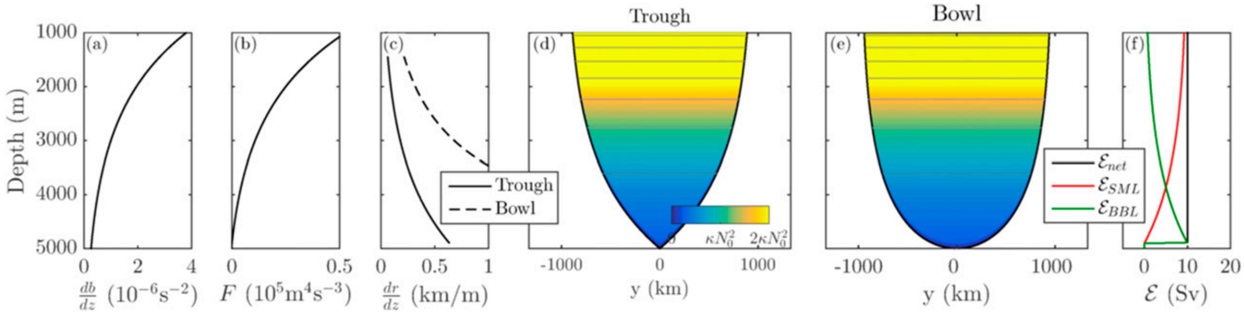

FIG. 7. As in Fig. 4, but for a constant interior diffusivity κ and exponentially increasing stratification.

at the crest of the seamount, to balance the inflow above the seamount. Notice that while there is no net dianeutral transport below the crest of the seamount, there are strong exactly canceling flows within the BBL and SML (green and red lines in Fig. 8f).

Below the crest of the ridge there is strong upwelling that increases approaching the crest, as a consequence of the peak in F at the crest. This implies that there are strong lateral inflows below the crest of the ridge as well as above. Mass conservation with a steady-state buoyancy field then requires that the ridge crest be a strong lateral source of fluid (Fig. 8g and orange arrows in Fig. 8b). Previously, it has been suggested that fluid upwells diabatically up to the crests of midocean ridges as a consequence of strong mixing along their flanks, followed by lateral adiabatic flows connected to the adiabatic upwelling in the Southern Ocean (e.g., Ferrari 2014). However, this argument is not complete since strong mixing can drive net downwelling just as easily as it can drive net upwelling. Our calculations here show that lateral adiabatic outflow at the level of ridge crests is more likely a consequence of the large area of mixing available at the crest of the ridge acting as a vertical attractor for dianeutral transport. Note also that the crest outflow occurs at the level where the ridge's area is at a maximum; this level is typically about 3000-m depth for the main ridges of the Pacific, Atlantic, and Indian Oceans (see section 5).

While the structure of $\mathcal{E}_{\text{net}}$, and thus the lateral flows, associated with a seamount or ridge can be complex, there are some overall constraints on this structure. For example, the yellow control volume shown in Fig. 8b, whose top edge lies well above the crest where $\mathcal{B}$ is weak, must lose buoyancy as a result of the diffusive buoyancy flux at its bottom edge. This diffusive buoyancy loss must be balanced by a net advective buoyancy flux into the domain associated with both the lateral flows and any nonzero $\mathcal{E}_{\text{net}}$ at the bottom edge of the control volume. This means that the average density of seawater entering the control volume via these flows must be less than the average density of water exiting the domain. In other words, *on average* the inflows must be more buoyant and lie above the outflows, with downwelling required to connect these flows.

Here and in section 3 we have examined how the dianeutral upwelling and the topography, respectively, are determined by the other parameters. A third possibility (considered in appendix B and Fig. B1) is how the stratification is determined from specified topography

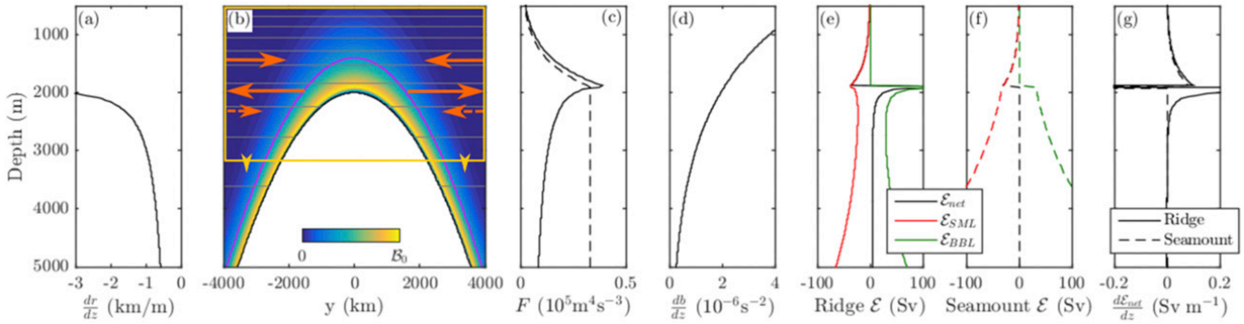

FIG. 8. The dianeutral circulation for a (e) ridge and (f) seamount with a (a),(b) parabolic topography $h(y) = z_0 - (y^2/a^2)$ and (d) exponentially increasing stratification. (c) The area-integrated buoyancy flux F obtained by integrating the buoyancy flux shown in (b) at constant height. (g) The vertical divergence of the net dianeutral transport, or the lateral inflow toward the ridge/seamount from the interior. These lateral flows are also indicated schematically in (b) by the orange arrows, where the inflow below the crest (dashed arrows) is only present for the ridge. The yellow box indicates a control volume over which there must be net diffusive buoyancy loss due to the loss of buoyancy through its bottom edge, which is balanced by an advective buoyancy flux into the control volume.

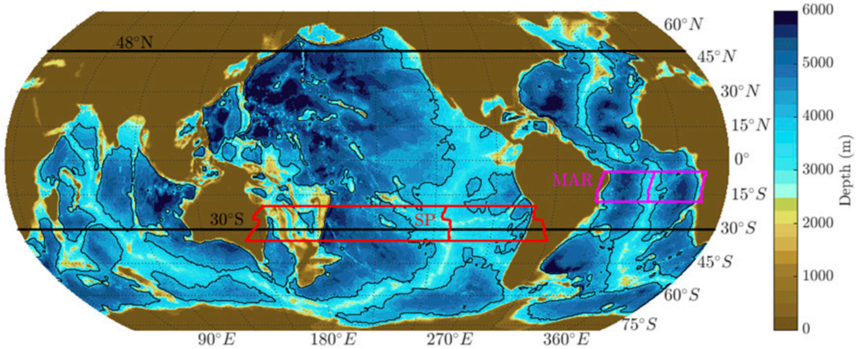

FIG. 9. Global ocean topography at 1/2° resolution from the 1/30° ETOPO2v2 dataset (Smith and Sandwell 1997). The 4000-m contour is plotted in black. The magenta and red areas show the MAR and SP regions considered in Fig. 10. The horizontal black lines show the latitude bounds used in Figs. 11 and 12.

and dianeutral upwelling profiles. We find that in many cases these solutions predict vanishing stratification, illustrating how nontrivial it is for the interior ocean to obtain a smooth, height-increasing stratification under the constraints of topography and a bottom-intensified buoyancy flux. In reality the stratification itself will influence the mixing. In particular, the unstratified solutions presented in appendix B cannot support a nonzero buoyancy flux as the mixing efficiency will reduce to zero. Introducing a stratification-dependent mixing efficiency would presumably result in solutions with weak stratification rather than vanishing stratification in these regions. However, such calculations are outside the scope of this article and will be left to future work.

5. Two-dimensional examples: The Mid-Atlantic Ridge and the South Pacific

In this section we examine how the ideas developed above apply to two more realistic topographies, namely, two-dimensional segments of the Mid-Atlantic Ridge and the South Pacific. We apply the same approach as in the previous section to derive the dianeutral transports, but this time from realistic topography and stratification. Our aim here is not to examine in detail the water-mass transformation associated with specific basins but instead to gain a qualitative understanding of the influence of their geometry on the dianeutral circulation. We use the 1/30° ETOPO2v2 dataset (Smith and Sandwell 1997) regridded at 1/2°.

a. *The Mid-Atlantic Ridge*

We first consider the relatively two-dimensional South Atlantic Ridge between 18° and 5°S (magenta region in Fig. 9). We calculate an average zonal cross section by averaging together ridge-centered zonal profiles of topography at each latitude in this range (Fig. 10a). At each zonal location we then apply a bottom-intensified vertical profile for the buoyancy flux per unit area [Eqs. (4) and (5)] to obtain a two-dimensional buoyancy flux structure similar to the idealized 2D examples discussed earlier (color in Fig. 10a). We then integrate this buoyancy flux at constant height over a number of different sectors of the basin (red, black, green and blue sectors in Fig. 10a) to obtain the area-integrated buoyancy flux $F^z(z)$ in each sector (corresponding colored lines in Fig. 10b). Once again, in order to focus only on the role of seafloor geometry we have assumed that the maximum magnitude of the buoyancy flux $\mathcal{B}_0$ is horizontally uniform.

If buoyancy were only a function of height, the sign of dF^z/dz determines whether the net dianeutral transport is upward ($dF^z/dz > 0$) or downward ($dF^z/dz < 0$). Of course in reality the buoyancy and stratification vary horizontally. In section 5a(2) we examine how our conclusions are altered when taking into account the observed lateral variations of neutral density γ in these regions by integrating the buoyancy flux along surfaces of constant γ [yielding $F^\gamma(\gamma)$]. However, it is informative to first consider integration of the buoyancy flux at constant height, equivalent to assuming that neutral density depends only on height, in order to isolate the role of seafloor geometry from the geometry of neutral density surfaces. The superscript z or γ on F is used to distinguish between these two cases.

We also note that the relationship between F and the sign of $\mathcal{E}_{\mathrm{net}}$ holds in each sector of the basin individually, as Eq. (2) applies to local as well as global regions (as emphasized by McDougall and Ferrari 2017).

1) AREA INTEGRATION AT CONSTANT HEIGHT

On both sides of the South Atlantic F^z increases rapidly with height from zero at the bottom (~5400 m), driving

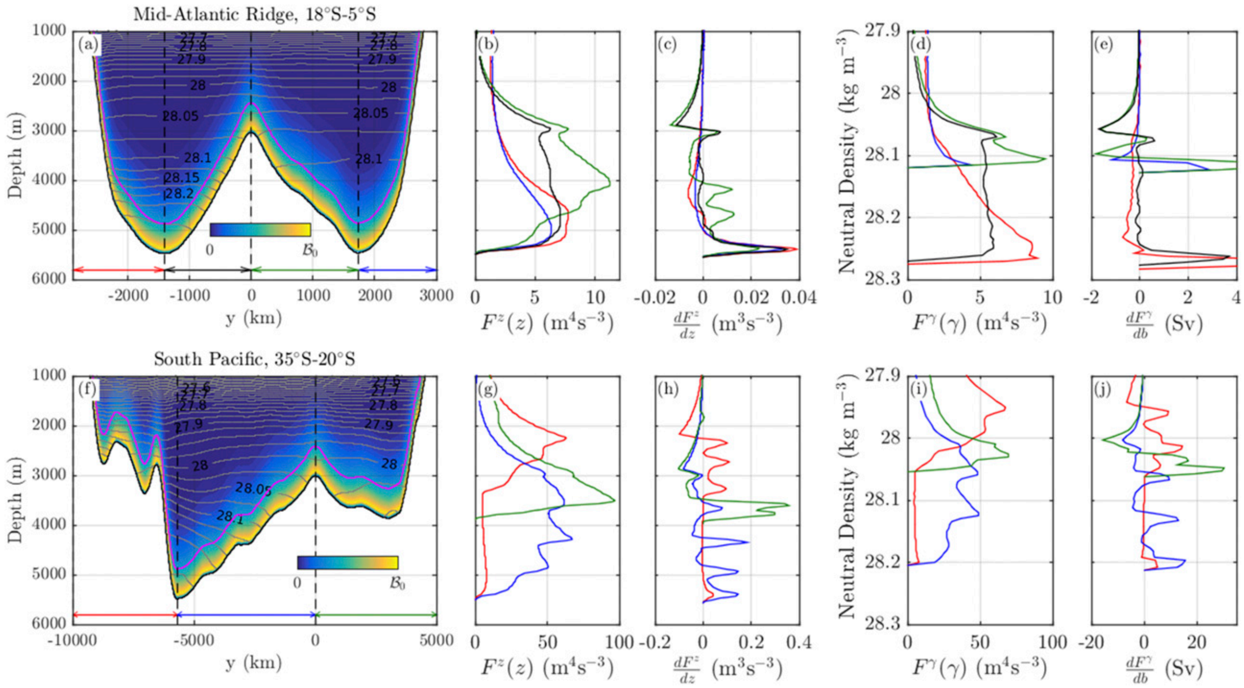

FIG. 10. Cross section of averaged topography across the (a) Mid-Atlantic Ridge between 18° and 5°S (magenta region in Fig. 9) and (f) the South Pacific between 35° and 20°S (red region in Fig. 9). In color is shown the assumed bottom-intensified buoyancy flux per unit area with scale height $d = 500$ m. In gray are contours of neutral density. The Atlantic cross section is split into four sectors corresponding to the Brazilian coast (red), the western ridge (black), the eastern ridge (green), and the African coast (blue). The South Pacific cross section is split into three sectors. (b),(g) The area-integrated buoyancy flux $F^z(z)$ at constant depth for the different sectors. (c),(h) The vertical derivative of $F^z(z)$. (d),(i) The area-integrated buoyancy flux $F^\gamma(\gamma)$ along neutral density surfaces. (e),(j) The net dianeutral mass flux $\mathcal{E}_{net} = dF^\gamma/db$.

upwelling there (Fig. 10c). On the continental slopes, F^z then decreases above 5000 m associated with a continuous steepening of the continental slopes (red and blue lines in Fig. 10b). This indicates that, without variations in the peak mixing intensity $\mathcal{B}_0$, continental slopes tend to be sites of net downwelling rather than upwelling. This statement also holds for the western side of the Mid-Atlantic Ridge (black lines in Figs. 10b,c), although the vertical variation in the slope is weaker here and thus we would expect weaker net dianeutral transport. However, the eastern side of the ridge has a section where the slope decreases with height extending the near-bottom upwelling up to 4000 m, with downwelling above (green lines in Figs. 10b,c). Of course, variations in $\mathcal{B}_0$ with height, if strong enough, can override these geometric effects.

The ridge crest is also an interesting feature. Because it is relatively flat, there must be an increase in A_{mix}, and thus F^z, approaching the crest (black and green lines in Fig. 10b near 3000 m). As discussed in section 4, this drives upwelling below the crest, which when combined with the downwelling that must occur above the crest, results in a vertical convergence of flow at the crest (Fig. 10c, near 3000 m). Thus, the ridge crest is a lateral source of fluid that must be removed by the adiabatic arm of the overturning circulation. Note that if mixing were enhanced at the crest, as suggested by some studies (St. Laurent and Thurnherr 2007; Lefauve et al. 2015), then this effect would be further enhanced.

2) AREA INTEGRATION ALONG NEUTRAL DENSITY SURFACES

We now perform a similar analysis, this time taking into account the lateral variations in neutral density γ by integrating the buoyancy flux along neutral density surfaces (gray lines in Fig. 10a), as calculated from the WOCE climatology (Gouretski and Koltermann 2004) using the method of Jackett and McDougall (1997). The neutral density surfaces slope downward as they intersect topography, a consequence of the no-flux boundary condition (Thompson and Johnson 1996; Garrett 2001). The vertical gradients in F^γ are compressed into narrow neutral density ranges, particularly in the deep eastern basin where the stratification is very weak (green and blue lines in Fig. 10d). There is large inferred upwelling in the densest waters in both basins where F^γ increases rapidly (Fig. 10e). Of course, upwelling in the eastern basin is likely to be reduced if a mixing efficiency dependence on db/dz was introduced (de Lavergne et al. 2016a; Mashayek et al. 2017). The convergence of $\mathcal{E}_{\mathrm{net}}$ at the ridge crest is also evident (green and black lines near 28.075 kg m^{-3} in Fig. 10e). Therefore we find that in terms of the sign of net dianeutral transport, there are only minor differences between integration along depth and neutral density surfaces within each coherent sector, implying that the departure of neutral density surfaces from the horizontal does not dramatically alter the conclusions reached in the previous section (cf. Figs. 10b and 10d).

The strong increase in F within the deepest part of the basins suggests that the dF/dz term in Eq. (7) dominates over F/d in this region. This contrasts with the simple geometrical configurations considered in section 3, where the assumption of constant $\mathcal{E}_{\mathrm{net}}$, and a smooth db/dz, drove F to increase slowly with height. The smallness of F/d compared with dF/dz means that the dianeutral transport in the interior $\mathcal{E}_{\mathrm{SML}}$ is small and that the net transport $\mathcal{E}_{\mathrm{net}}$ is mostly associated with the transport in the BBL. This dominance of dF/dz over F/d also suggests that the constant buoyancy flux per unit area regime discussed in section 3d applies reasonably well in these bottom-most regions (since there is a finite buoyancy flux throughout depths within d of the basin bottom such that bottom-intensified and constant buoyancy flux regimes are similar), where much of the dianeutral upwelling may occur. The results of de Lavergne et al. (2017) also support this conclusion, with their constant buoyancy flux scenario reproducing the peak in global dianeutral upwelling at 28.11 kg m^{-3} predicted by the inverse calculation of Ganachaud and Wunsch (2000) and implied by the Pacific radiocarbon distribution.

b. The South Pacific

The Pacific is generally more topographically complex than the Atlantic. As an example, we consider a relatively two-dimensional zonal segment in the South Pacific between 35° and 20°S, centered on the East Pacific Rise (red region in Fig. 9). The topography along this segment has gentler slopes than the Atlantic segment, apart from the steep western side of the Tonga–Kermadec trench (cf. Figs. 10f and 10a, where the horizontal scale is 2.5 times larger in Fig. 10f). These gentle slopes and the larger zonal extent in comparison to the Atlantic segment result in a much larger area-integrated buoyancy flux F (cf. Figs. 10g,i with Figs. 10b,d, respectively; the meridional extent of the two regions is similar). Nevertheless, many of the qualitative features characterizing the Atlantic segment are also true here. There is large buoyancy gain and upwelling in the deepest, densest waters. The convergence of dF/dz at the crest of the East Pacific Rise (green and blue lines near 3000 m in Fig. 10h) is also evident, but less prominent than for the Mid-Atlantic Ridge.

6. Is the ocean two-dimensional or three-dimensional?

Given the discussion in the earlier sections of this article, the question arises as to whether the ocean, on average, can be thought of as two-dimensional or three-dimensional and axis-symmetric. Previous authors have considered the global ocean in an idealized sense as a 3D bowl (Rhines and MacCready 1989; McDougall and Ferrari 2017) or 2D trough (Ferrari et al. 2016). In this section we ask whether these idealizations are appropriate. In the process, we examine what controls vertical variations in the incrop area of density layers, known to be crucial to the abyssal dianeutral circulation (de Lavergne et al. 2016b, 2017).

We first continue to assume that neutral density varies only with height to focus on the influence of seafloor geometry on variations in the incrop area independently of the neutral density surface geometry and the climatology or climate associated with a given neutral density distribution (section 6a). Later (section 6b), we return to buoyancy space using the WOCE climatology and show that, as in the specific examples in the previous section, the results are not qualitatively different.

a. The incrop area of depth layers

Assuming that buoyancy varies only with height and that mixing is bottom intensified with uniform peak magnitude, the incrop area of depth layers into the topography dA/dz controls the area-integrated buoyancy flux F and thus the sign of the net dianeutral transport $\mathcal{E}_{\mathrm{net}}$. As discussed in section 2, when the topography and F change slowly in the vertical (with respect to d) F/d dominates dF/dz in Eq. (7). Combining Eqs. (7), (9), and (6) in this limit,

$$\mathcal{E}_{\mathrm{net}}(z) \approx \mathcal{B}_0 d \left(\frac{db}{dz}\right)^{-1} \frac{d}{dz}\left(\frac{dA}{dz}\right). \tag{25}$$

That is, the sign of $\mathcal{E}_{\mathrm{net}}$ is controlled by the vertical derivative of the incrop area dA/dz. Net dianeutral upwelling occurs when the incrop area increases with height $[d/dz(dA/dz) > 0]$, and net dianeutral downwelling occurs when the incrop area decreases with height $[d/dz(dA/dz) < 0]$. Below, we assess whether it is changes in the slope or the perimeter of bathymetric contours with height that plays the dominant role in driving these vertical variations in dA/dz.

It is also worth noting that if the buoyancy flux per unit area were constant in the interior instead of bottom intensified (as considered in section 3d), then dF/dz dominates F/d in Eq. (7), and Eq. (25) is replaced by

$$\mathcal{E}_{\mathrm{net}}(z) \approx \mathcal{B}_0 \left(\frac{db}{dz}\right)^{-1} \frac{dA}{dz}. \tag{26}$$

In this case the incrop area directly controls the sign of $\mathcal{E}_{\mathrm{net}}$, rather than its vertical derivative.

We consider the global topography between 30°S and 48°N. We calculate both the total ocean area $A(z)$ and the global length of the bathymetric contour, or the perimeter $L(z)$, at each height. Given $L(z)$ and $A(z)$ we can derive an effective inverse slope $\overline{dr/dz}$ by rearranging Eq. (9):

$$\overline{\frac{dr}{dz}} = \frac{1}{L(z)}\frac{dA}{dz}. \qquad (27)$$

This quantifies the contribution of changes in the average sidewall slope to changes in area with height. An effective radial profile can then be obtained by integration:

$$\overline{r}(z) = \int_{z_0}^{z} \overline{\frac{dr}{dz}}\, dz, \qquad (28)$$

where we use $z_0 = -6500$ m. Note that the calculation of the length of a bathymetric contour is resolution dependent. The relevant length scale is the width of the SML, which depends on the topographic slope. To sufficiently capture the steep continental slopes, we choose a 1/2° bathymetric grid, which for a decay scale of $d = 500$ m corresponds to a slope of $\sim 1/100$ (appropriate for the African continental slope in Fig. 10a). While the magnitude of the perimeter and effective inverse slope do change with resolution, their qualitative form does not, and the conclusions below are not altered.

There is a distinct peak in the incrop area between 4000 and 5500 m (Fig. 11b). There are strong variations in both perimeter and slope that contribute to dA/dz (black lines in Figs. 11a,c). The perimeter increases up to 4200 m (i.e., bowl-like behavior) and then decreases above (i.e., seamount-like behavior) due to the disappearance of ridges and seamounts. However, the height of maximum perimeter and maximum dA/dz are offset from each other, owing to the influence of the slope. Over the majority of the depth range the effective slope is increasing (Fig. 11c).

For bottom-intensified mixing the sign of the vertical derivative in the incrop area d^2A/dz^2 determines the sign of $\mathcal{E}_{\mathrm{net}}$ if neutral density varies only with height [Eq. (25)]. We can split d^2A/dz^2 into two terms:

$$\frac{d^2A}{dz^2} = \frac{dL}{dz}\overline{\frac{dr}{dz}} + L\frac{d}{dz}\left(\overline{\frac{dr}{dz}}\right), \qquad (29)$$

associated with changes in the perimeter and slope, respectively. This decomposition shows that the increase in incrop area with height below 4500 m is entirely driven by the increase in the perimeter of bathymetric contours (cf. black dashed and solid lines in Fig. 11e). In contrast, the reduction in incrop area between 4400 and 2000 m is largely driven by the continuous increase in the effective slope (cf. black dotted and solid lines in Fig. 11e) transitioning from the flat abyssal plains to the steep continental slopes (e.g., Fig. 10a). Hence, vertical variations in the perimeter and slope promote upwelling below 4500 m and downwelling above, respectively (remembering, of course, that the connection to upwelling and downwelling relies on the assumption of a constant $\mathcal{B}_0$). If on the other hand the buoyancy flux per unit area was constant in the interior [Eq. (26)], then the downwelling above 4500 m would be replaced by weakening upwelling (de Lavergne et al. 2017), driven again by the increase in the slope.

For comparison purposes, we also estimate the perimeter and slope for 2D (i.e., a constant perimeter; red lines in Fig. 11) and 3D axis-symmetric [i.e., the perimeter $L = 2\pi\overline{r}$, where $\overline{r}$ is the effective radial profile in Eq. (28); green lines in Fig. 11] oceans with the same incrop area. These 2D and 3D oceans are fundamentally different from the real ocean. For the 2D ocean, changes in incrop area are entirely driven by changes in the slope. Consequently, the slope must be comparatively steep below 5500 m, gentle between 5500 and 3000 m, and steeper above, relative to the real ocean with a variable perimeter (cf. red and black lines in Figs. 11c,d). This is similar to the differences near the bottom of the domain between the trough and bowl shown in section 3 (e.g., cf. Fig. 4d and Fig. 4e). The 3D axis-symmetric ocean also shows some drastic departures from reality: the 3D ocean perimeter must always increase with height. While this may be accurate in the abyssal ocean below 4000 m, it is not realistic elsewhere. Also, since an axis-symmetric system is the one with minimum perimeter for a given area, both the perimeter and consequently the slope are much smaller than the other two cases (note the order-of-magnitude difference between the green and black lines in Figs. 11c,d).

Note that the qualitative results discussed above are not sensitive to the basin considered. While there are some quantitative differences, the overall properties linked to the geometry the abyssal plains, ridges, and continental slopes are consistent across the three main ocean basins.

b. *The incrop area of neutral density layers*

We now extend the results of the previous section to the general case of curved neutral density surfaces. As discussed by de Lavergne et al. (2016b), the incrop area of neutral density layers $-dA/d\gamma$ exerts a strong constraint on the net dianeutral transport. When mixing is

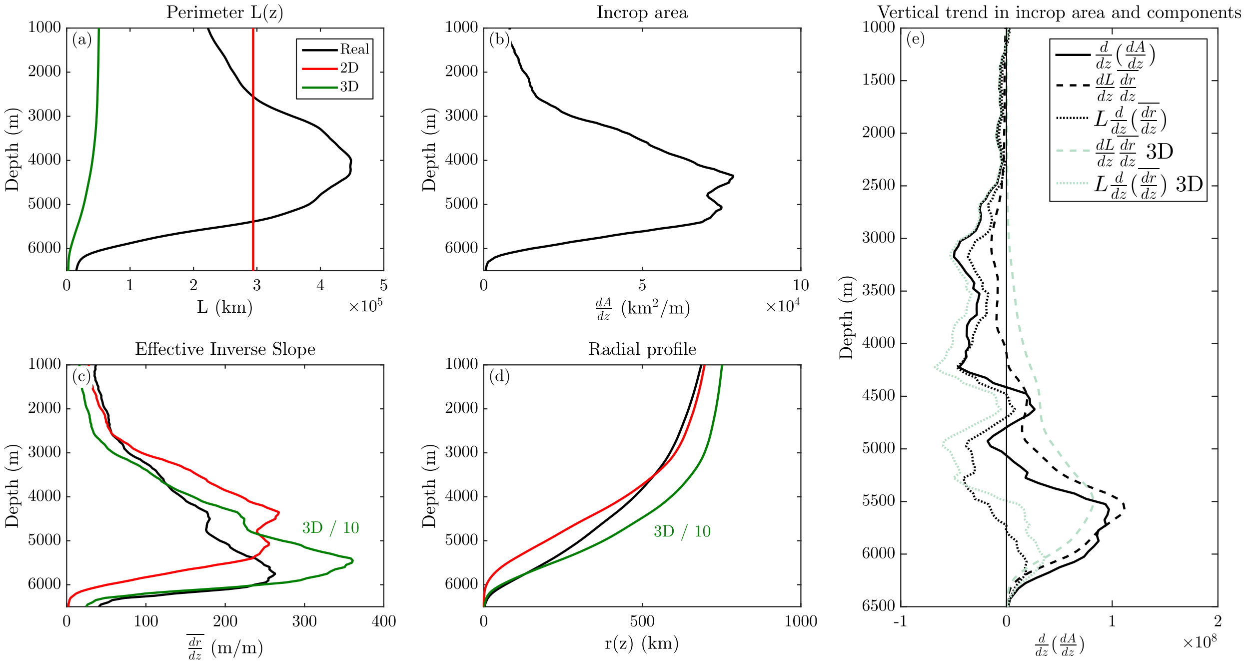

FIG. 11. Properties of the seafloor topography between 30°S and 48°N using 1/2° resolution topography. (a) Perimeter $L(z)$, (b) incrop area of depth layers, (c) the effective inverse slope $\overline{dr/dz}$ [Eq. (27)], (d) the radial profile obtained from $\overline{dr/dz}$, and (e) the vertical trend in incrop area (solid black) and the contributions of variations in perimeter (dashed black) and inverse slope (dotted black) to that trend. In red is the 2D case where the perimeter is constant and equal to the average of the real perimeter. In green is the 3D axis-symmetric case characterized by $L = 2\pi r$ [this case is also shown with faint lines in (e)]. Note the order of magnitude difference between the 3D case and the others in (c) and (d).

bottom intensified, layers with a larger incrop area are exposed to larger buoyancy fluxes. Therefore these layers host a larger area-integrated buoyancy flux F, which controls $\mathcal{E}_{\mathrm{net}}$ through Eq. (2). Here, we perform a similar decomposition as in the previous section [e.g., Eqs. (25), (27), and (29), with d/dz replaced by $-d/d\gamma$ except in db/dz] where the perimeter L is now replaced by the length of the outer edge of a given neutral density surface where it comes into contact with the seafloor. The effective inverse slope $-\overline{dr/d\gamma}$ is now interpreted as the average inverse slope of the topography in density space, which includes both the effects of a sloping seafloor and the geometry of neutral density surfaces.

The incrop area of density layers is confined to a narrow range of neutral densities between 28 and 28.2 kg m^{-3} (Fig. 12b). This is a result of the large volume of weakly stratified waters with neutral density near 28.11 kg m^{-3} that cover much of the abyssal plains (de Lavergne et al. 2016b). The decomposition of the incrop area into the perimeter (black line in Fig. 12a) and effective inverse slope (black line in Fig. 12c) in density space is nevertheless qualitatively similar to that in depth space. The increase in incrop area below 28.11 kg m^{-3} is driven by a rapid increase in the perimeter of neutral-density surfaces (cf. dashed and solid black lines in Fig. 12e), while the decrease above 28.11 kg m^{-3} is driven by a rapid decrease in the effective slope of topography in density space (cf. dotted and solid black lines in Fig. 12e).

To recap, we find that the real ocean does not map onto any single purely 2D or 3D axis-symmetric geometry. However, in certain depth or density ranges these idealized geometries do describe the real ocean reasonably well. Below the incrop area peak near 4000 m, the increasing perimeter plays an important role suggesting that the ocean acts like a 3D bowl, albeit with a much larger circumference relative to its area. Above 4000 m changes in the perimeter are much weaker, and the main geometrical feature is the increase in the average slope, suggesting that the 2D trough idealization is more appropriate.

7. Summary and discussion

We have examined the relationship between the geometry of the seafloor and the abyssal dianeutral circulation when buoyancy fluxes per unit area are bottom intensified and of uniform bottom magnitude. Conclusions can be summarized as follows:

1) Under an assumption of vertically uniform net dianeutral upwelling, subtle differences in the slope and circumference of the seafloor can result in

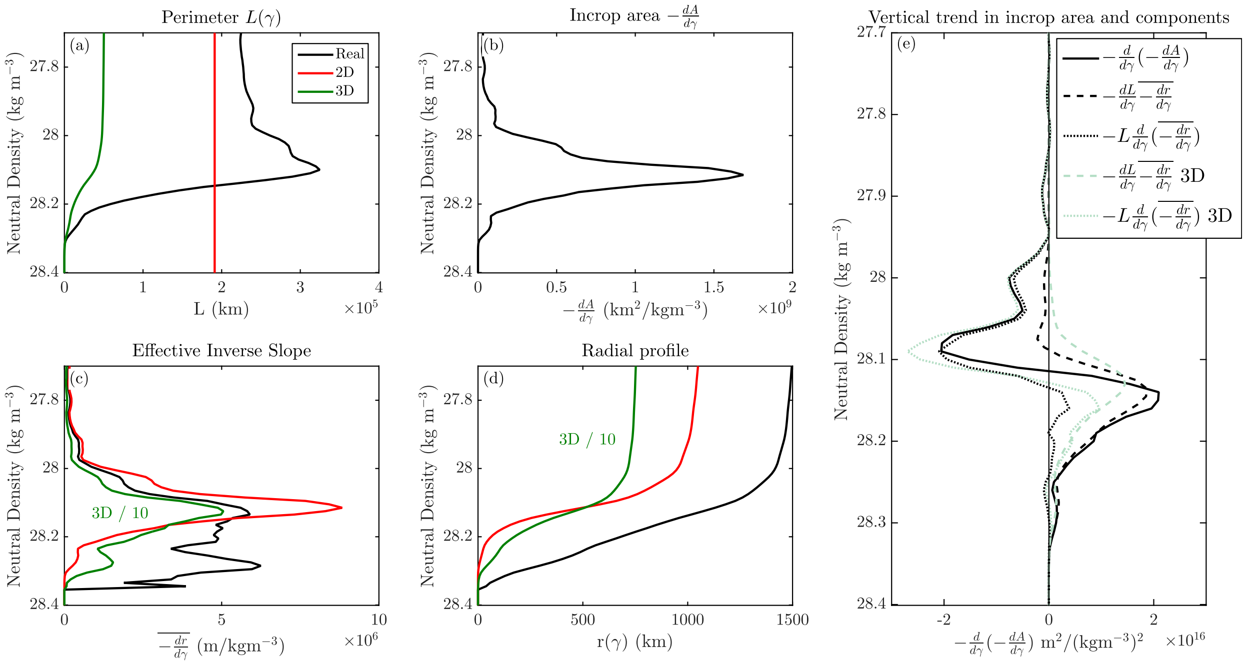

FIG. 12. As in Fig. 11, but for neutral density space calculated using the WOCE climatology.

stratification that is bottom intensified, uniform, or surface intensified (Fig. 4).

The sensitivity of the interior stratification to the seafloor geometry raises the following question: Why does the abyssal stratification increase relatively smoothly in the vertical? The answer likely involves a coupling between the topographic effects discussed here, the vertical structure of the lateral flows to and from the Southern Ocean (and the North Atlantic), and spatial variations in mixing intensity.

2) Variations in topography can drive lateral, adiabatic flows away from and toward topographic features. The crests of midocean ridges may be particularly strong sources of lateral flow because the area of active mixing is highest near the ridge crest, driving a convergence of the net dianeutral transport there.
3) Geometric considerations suggest that much of the diabatic upwelling may occur near the bottom of the ocean basins (e.g., South Atlantic and South Pacific segments in Fig. 10). The densest waters residing at the bottom of these basins are best placed to be consumed by the bottom-intensified turbulence, owing to the large seafloor area and the large area-integrated buoyancy flux that converges there. This suggests that AABW consumption is essentially a sequential and lateral (rather than vertical) phenomenon, with the density of peak consumption moving to progressively lighter densities as AABW moves northward away from the Southern Ocean and becomes more homogeneous (de Lavergne et al. 2016b, 2017).
4) Finally, changes in the perimeter of global neutral-density surfaces dominate the increase with height of the incrop area of neutral density layers below 4500 m (Figs. 11 and 12). As the vertical derivative of this incrop area is a key determinant of the net dianeutral transport owing to the bottom-enhanced turbulence, much of the net dianeutral upwelling below 4500 m may be associated with this increase in perimeter. In contrast, the effective slope of the seafloor increases with height throughout the deep ocean, associated with the transition from flat abyssal plains to steep continental slopes, driving a decrease in the incrop area above 4500 m. This implies that the geometry in this depth range is prone to net dianeutral downwelling. If net upwelling is to be achieved here then it must be through a height increase of the mean intensity of boundary mixing as measured by $\mathcal{B}_0$, or by a buoyancy flux per unit area that does not decay above the bottom, or by geothermal heating. It is worth noting that if the diffusivity at the top of the BBL were constant then the increasing stratification with height will result in an increasing $\mathcal{B}_0$ with height that is favorable for net upwelling.

The main drawbacks of the approach taken in this article are the assumptions of horizontally homogeneous stratification, a constant mixing efficiency Γ, and no lateral variations in the peak buoyancy flux $\mathcal{B}_0$. In particular, variations in $\mathcal{B}_0$ may be expected to have a large impact. We have also ignored the multiple effects of the nonlinear nature of the equation of state of seawater (Klocker and McDougall 2010). These assumptions allowed us to obtain simple solutions and isolate the role of topography. Future work will attempt to address these drawbacks, in particular to allow for feedbacks between the stratification and the buoyancy flux. Additionally, we have not considered the role of mixing processes along neutral density surfaces, such as mesoscale eddies. These may play an important role by altering the geometry of neutral density surfaces and the structure of the boundary layer (e.g., Broadbridge et al. 2016).

Acknowledgments. We gratefully acknowledge support from the Australian Research Council through Grant FL150100090.

APPENDIX A

Mathematical Details

a. *Derivation of Eq. (7)*

Equation (6) can be solved for the topography $h(y)$ by combining Eqs. (3) and (5):

$$F(z) = \mathcal{B}_0 \int_{y_0}^{r(z)} L(y) \exp\left[-\frac{z - h(y) - h_{\rm BBL}}{d}\right] dy\,. \qquad \text{(A1)}$$

The integral in Eq. (A1) begins at $y_0 = 0$, where $F = 0$ and the depth is $h(y_0) = -H$ (see Fig. A1). Equation (A1) applies to both 2D and 3D geometries. We have ignored the contribution of the buoyancy flux within the BBL to F, as this is small [because the layer is well-mixed, neutral-density surfaces are approximately perpendicular to the topography so that the buoyancy gradient along the topography is small and thus the area is also small; also see Kunze et al. (2012) and McDougall and Ferrari (2017)]. The function $y = r(z)$ is the inverse function of $z = h(y) + h_{\rm BBL}$ (Fig. A1). To obtain a solution we require that $h(y)$ is a monotonic function of y [so that $r(z)$ exists]. Equation (A1) can be solved for the inverse slope of the topography dr/dz through a derivative with respect to z and application of the Leibniz rule, yielding Eq. (7).

b. *The area of the SML $A_{\rm mix}$*

The area of the SML $A_{\rm mix}$ (McDougall and Ferrari 2017) can be defined as the horizontal area between the top of the BBL and the contour a distance d above the BBL (Fig. A1):

$$A_{\rm mix}(z) \equiv \int_{r(z-d)}^{r(z)} L(y)\, dy\,. \qquad \text{(A2)}$$

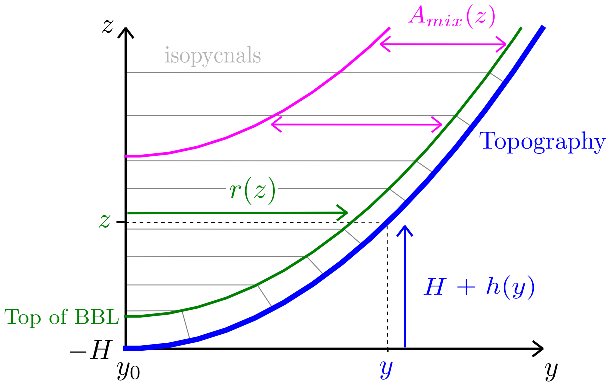

FIG. A1. The coordinates used to solve for the topography in the simple 2D and circular geometries. The $h(y)$ is the (negative) height of topography and $r(z)$ is the distance from y_0 to the top of the BBL. Also shown is the width of the SML $A_{\rm mix}(z)$; the distance between the top of the BBL and the point at which the buoyancy flux has decreased by a factor of $1/e$.

In the case where both L and dr/dz change slowly in the vertical with respect to d [i.e., the slope curvature $d/dz(dr/dz)^{-1} \ll (1/d)(dr/dz)^{-1}$], this reduces to

$$A_{\rm mix} \approx L[r(z) - r(z-d)] \approx Ld\frac{dr}{dz} = d\frac{dA}{dz}\,. \qquad \text{(A3)}$$

c. *The trough, bowl, ridge, and seamount slopes for uniform dianeutral upwelling*

Here we derive the forms for the topographic slopes of the bowl, trough, ridge, and seamount geometries used in section 3. Using Eq. (12) in Eq. (8) with a constant $\mathcal{E}_{\rm net}$ yields the following:

$$F = s\mathcal{E}_{\rm net}N_0^2[e^{(z+H-h_{\rm BBL})/s} - 1], \quad \text{exponential}\ db/dz\,, \qquad \text{(A4)}$$

and

$$F = \mathcal{E}_{\rm net}N_0^2(z + H - h_{\rm BBL}), \quad \text{constant}\ db/dz\,. \qquad \text{(A5)}$$

Using Eqs. (A4) and (A5) in Eq. (7) yields the following:

$$L\frac{dr}{dz} = \frac{\mathcal{E}_{\rm net}N_0^2}{\mathcal{B}_0}\left[e^{(z+H-h_{\rm BBL})/s}\left(1 + \frac{s}{d}\right) - \frac{s}{d}\right], \quad \text{exponential}\ db/dz, \qquad \text{(A6)}$$

and

$$L\frac{dr}{dz} = \frac{\mathcal{E}_{\rm net}N_0^2}{\mathcal{B}_0}\left(1 + \frac{z + H - h_{\rm BBL}}{d}\right), \quad \text{constant}\ db/dz\,. \qquad \text{(A7)}$$

To obtain the topography $r(z)$, we then integrate with respect to z [for the circular geometries where $L = 2\pi r$, this involves first using the identity $L(dr/dz) = d/dz(\pi r^2)$].

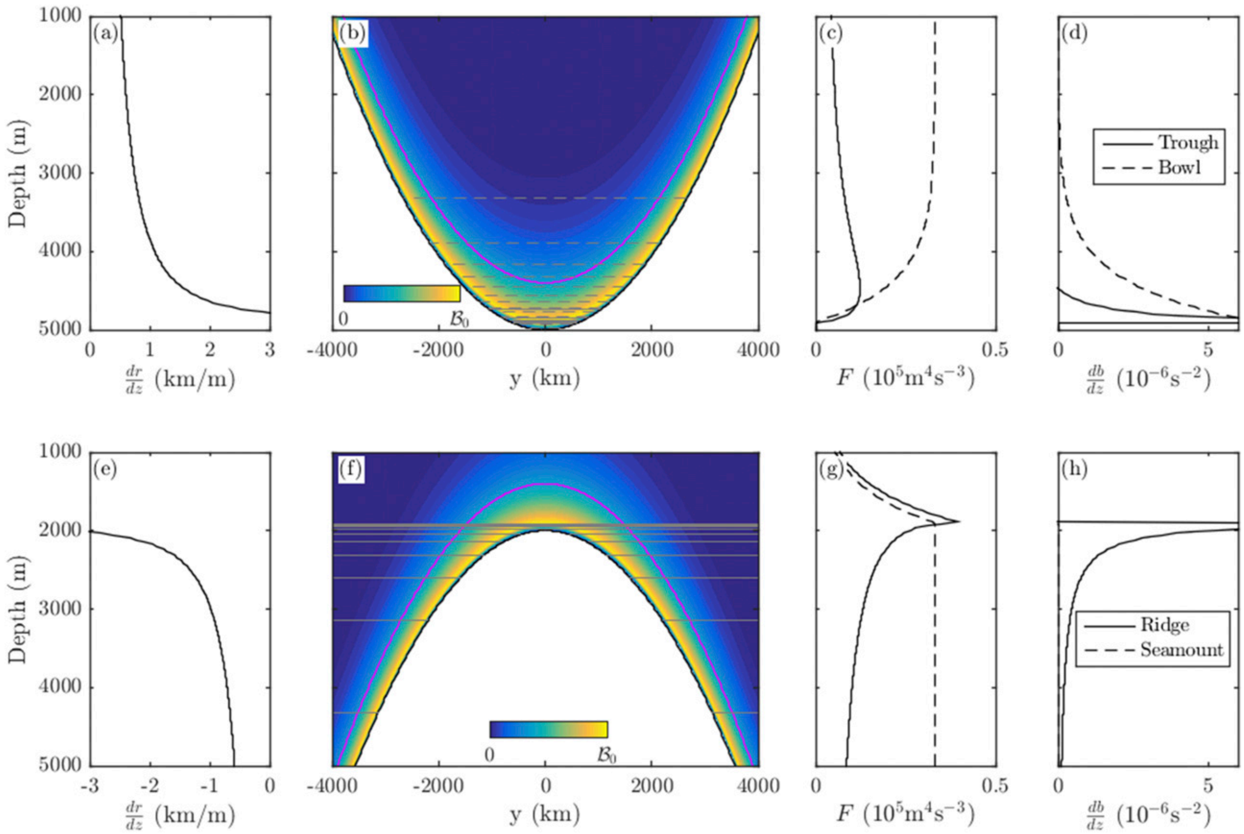

FIG. B1. The stratification (d),(h) obtained for a parabolic slope [$h(y) = z_0 \pm (y^2/a^2)$] with uniform net dianeutral upwelling for (a)–(d) the trough and bowl and (e)–(h) the ridge and seamount. In (b) and (f) neutral density contours for the 2D (solid contours) and 3D (dashed contours) geometries are shown in gray.

Equations (A6) and (A7) were obtained by assuming that $r(z)$ increases with height from zero at $z_0 = H - h_{\mathrm{BBL}}$ upward (appropriate for the trough and bowl geometries where $dr/dz > 0$). However, we can also multiply the RHS of Eqs. (A6) and (A7) by -1 and integrate downward from a shallower starting height z_0 to obtain a solution where $r(z)$ decreases with height (appropriate for the ridge and seamount geometries, where $dr/dz < 0$).

d. The area-integrated buoyancy flux for the parabolic ridge and seamount

The slope of the parabolic ridge and seamount corresponding to Eq. (24) considered in section 4 is given by

$$\frac{dr}{dz} = -\frac{a}{2\sqrt{z_0 + h_{\mathrm{BBL}} - z}}. \tag{A8}$$

Given this slope, the area-integrated buoyancy flux around the ridge [using Eq. (A1)] is

$$F_{\mathrm{ridge}} = 2L_c\mathcal{B}_0\int_{r(z)}^{\infty}\exp\left[-\frac{z-h(y)-h_{\mathrm{BBL}}}{d}\right]dy,$$

$$=aL_c\mathcal{B}_0\sqrt{\pi d}e^{(z_0+h_{\mathrm{BBL}}-z)/d}\left[1-\mathrm{erf}\left(\sqrt{\frac{z_0+h_{\mathrm{BBL}}-z}{d}}\right)\right],$$

$$z<z_0, \quad \text{and} \tag{A9}$$

$$=aL_c\mathcal{B}_0\sqrt{\pi d}e^{(z_0+h_{\mathrm{BBL}}-z)/d}, \quad z>z_0, \tag{A10}$$

and around the seamount is given by

$$F_{\mathrm{seamount}}=2\pi\mathcal{B}_0\int_{r(z)}^{\infty}y\exp\left[-\frac{z-h(y)-h_{\mathrm{BBL}}}{d}\right]dy,$$

$$=\mathcal{B}_0\pi a^2 d, \quad z<z_0, \tag{A11}$$

$$=\mathcal{B}_0\pi a^2 d e^{(z_0+h_{\mathrm{BBL}}-z)/d}, \quad z>z_0. \tag{A12}$$

These relations are illustrated in Fig. 8, for the case of exponentially increasing stratification with height.

APPENDIX B

Steady-State Stratification Given a Constant Supply of Bottom Water

In this appendix we consider how the stratification is determined by the other parameters: the topography and net dianeutral transport. Without a supply of bottom water, there is no stratified steady-state solution, as the densest waters will be progressively consumed by mixing. Thus we will consider again the case of uniform net dianeutral upwelling forced by a source of bottom water at the base of the domain. As in section 4, we consider parabolic geometries. The situation considered here is relevant for example for a laboratory or numerical experiment where the topography, buoyancy flux, and inflow of bottom fluid are specified and the stratification must adjust.

The steady-state stratifications are quite different across the four cases of parabolic ridge, seamount (Fig. B1f), trough, and bowl (Fig. B1b) topographies. For the parabolic seamount, as noted in section 4, F is uniform below the crest and decreases above (dashed line in Fig. B1g). Thus there are no regions where F increases with height and the seamount cannot support upwelling through a positive stratification, forcing an unstratified solution. For the ridge topography, F increases with height below the ridge crest and so net dianeutral upwelling through a stable stratification can be supported there. The stratification must increase very rapidly toward the ridge crest in order to constrain upwelling to 10 Sv given the rapid increase in F (solid line in Fig. B1h). Note again that since F always decreases above the crest of the ridge or seamount, net upwelling through a stable stratification cannot be supported there and the fluid is unstratified.

For the bowl geometry, F increases from the bottom of the bowl upward, approaching a constant value well above the bottom (dashed line in Fig. B1c). Thus uniform upwelling can be supported provided that db/dz decays toward zero with height (dashed line in Fig. B1d). Finally, stratification can only be supported close to the bottom of the trough (solid line in Fig. B1d) where F increases (rapidly).

These results change if the buoyancy flux per unit area is assumed to be constant, with $d \to \infty$ (not shown). In this case, both the trough and bowl can support nonzero stratification throughout the entire depth range, as the total area of fluid always increases with height. In fact, the parabolic bowl with constant upwelling supports a uniform stratification (identical to the second row of Fig. 6), since the total area of the paraboloid increases linearly. The trough stratification is strongly peaked at the bottom of the basin, as for the bottom-intensified case, but decays exponentially more slowly in the vertical, approaching but never reaching zero.

REFERENCES

Broadbridge, M. B., A. C. Naveira Garabato, and A. J. G. Nurser, 2016: Forcing of the overturning circulation across a circumpolar channel by internal wave breaking. *J. Geophys. Res. Oceans*, **121**, 5436–5451, https://doi.org/10.1002/2015JC011597.

Bryden, H. L., and A. J. G. Nurser, 2003: Effects of strait mixing on ocean stratification. *J. Phys. Oceanogr.*, **33**, 1870–1872, https://doi.org/10.1175/1520-0485(2003)033<1870:EOSMOO>2.0.CO;2.

de Lavergne, C., G. Madec, J. Le Sommer, A. J. G. Nurser, and A. C. Naveira Garabato, 2016a: The impact of a variable mixing efficiency on the abyssal overturning. *J. Phys. Oceanogr.*, **46**, 663–681, https://doi.org/10.1175/JPO-D-14-0259.1.

——, ——, ——, ——, and ——, 2016b: On the consumption of Antarctic Bottom Water in the abyssal ocean. *J. Phys. Oceanogr.*, **46**, 635–661, https://doi.org/10.1175/JPO-D-14-0201.1.

——, ——, F. Roquet, R. M. Holmes, and T. J. McDougall, 2017: Abyssal ocean overturning shaped by seafloor distribution. *Nature*, **551**, 181–186, https://doi.org/10.1038/nature24472.

Dell, R. W., and L. J. Pratt, 2015: Diffusive boundary layers over varying topography. *J. Fluid Mech.*, **769**, 635–653, https://doi.org/10.1017/jfm.2015.88.

Emile-Geay, J., and G. Madec, 2009: Geothermal heating, diapycnal mixing and the abyssal circulation. *Ocean Sci.*, **5**, 203–217, https://doi.org/10.5194/os-5-203-2009.

Ferrari, R., 2014: Oceanography: What goes down must come up. *Nature*, **513**, 179–180, https://doi.org/10.1038/513179a.

——, M. F. Jansen, J. F. Adkins, A. Burke, A. L. Stewart, and A. F. Thompson, 2014: Antarctic sea ice control on ocean circulation in present and glacial climates. *Proc. Natl. Acad. Sci. USA*, **111**, 8753–8758, https://doi.org/10.1073/pnas.1323922111.

——, A. Mashayek, T. J. McDougall, M. Nikurashin, and J.-M. Campin, 2016: Turning ocean mixing upside down. *J. Phys. Oceanogr.*, **46**, 2239–2261, https://doi.org/10.1175/JPO-D-15-0244.1.

Ganachaud, A., and C. Wunsch, 2000: Improved estimates of global ocean circulation, heat transport and mixing from hydrographic data. *Nature*, **408**, 453–457, https://doi.org/10.1038/35044048.

Garrett, C., 1990: The role of secondary circulation in boundary mixing. *J. Geophys. Res.*, **95**, 3181–3188, https://doi.org/10.1029/JC095iC03p03181.

——, 1991: Marginal mixing theories. *Atmos.–Ocean*, **29**, 313–339, https://doi.org/10.1080/07055900.1991.9649407.

——, 2001: An isopycnal view of near-boundary mixing and associated flows. *J. Phys. Oceanogr.*, **31**, 138–142, https://doi.org/10.1175/1520-0485(2001)031<0138:AIVONB>2.0.CO;2.

——, and E. Kunze, 2007: Internal tide generation in the deep ocean. *Annu. Rev. Fluid Mech.*, **39**, 57–87, https://doi.org/10.1146/annurev.fluid.39.050905.110227.

Gouretski, V., and K. P. Koltermann, 2004: WOCE global hydrographic climatology. Berichte des Bundesamtes für Seeschifffahrt und Hydrographie 35, 52 pp., https://odv.awi.de/fileadmin/user_upload/odv/data/Gouretski-Koltermann-2004/BSH35_report_final.pdf.

Gregg, M., E. D'Asaro, J. Riley, and E. Kunze, 2018: Mixing efficiency in the ocean. *Annu. Rev. Mar. Sci.*, **10**, 443–473, https://doi.org/10.1146/annurev-marine-121916-063643.

Holmes, R. M., J. N. Moum, and L. N. Thomas, 2016: Evidence for seafloor-intensified mixing by surface-generated equatorial waves. *Geophys. Res. Lett.*, **43**, 1202–1210, https://doi.org/10.1002/2015GL066472.

Hughes, G., and R. Griffiths, 2006: A simple convective model of the global overturning circulation, including effects of entrainment into sinking regions. *Ocean Modell.*, **12**, 46–79, https://doi.org/10.1016/j.ocemod.2005.04.001.

Iudicone, D., G. Madec, and T. J. McDougall, 2008: Water-mass transformations in a neutral density framework and the key role of light penetration. *J. Phys. Oceanogr.*, **38**, 1357–1376, https://doi.org/10.1175/2007JPO3464.1.

Ivey, G., K. Winters, and J. Koseff, 2008: Density stratification, turbulence, but how much mixing? *Annu. Rev. Fluid Mech.*, **40**, 169–184, https://doi.org/10.1146/annurev.fluid.39.050905.110314.

Jackett, D. R., and T. J. McDougall, 1997: A neutral density variable for the world's oceans. *J. Phys. Oceanogr.*, **27**, 237–263, https://doi.org/10.1175/1520-0485(1997)027<0237:ANDVFT>2.0.CO;2.

Klocker, A., and T. J. McDougall, 2010: Influence of the nonlinear equation of state on global estimates of dianeutral advection and diffusion. *J. Phys. Oceanogr.*, **40**, 1690–1709, https://doi.org/10.1175/2010JPO4303.1.

Kunze, E., 2017: Internal wave-driven mixing: Global geography and budgets. *J. Phys. Oceanogr.*, **47**, 1325–1345, https://doi.org/10.1175/JPO-D-16-0141.1.

——, C. MacKay, E. E. McPhee-Shaw, K. Morrice, J. B. Girton, and S. R. Terker, 2012: Turbulent mixing and exchange with interior waters on sloping boundaries. *J. Phys. Oceanogr.*, **42**, 910–927, https://doi.org/10.1175/JPO-D-11-075.1.

Ledwell, J. R., E. T. Montgomery, K. L. Polzin, L. C. St. Laurent, R. W. Schmitt, and J. M. Toole, 2000: Evidence for enhanced mixing over rough topography in the abyssal ocean. *Nature*, **403**, 179–182, https://doi.org/10.1038/35003164.

Lefauve, A., C. Muller, and A. Melet, 2015: A three-dimensional map of tidal dissipation over abyssal hills. *J. Geophys. Res. Oceans*, **120**, 4760–4777, https://doi.org/10.1002/2014JC010598.

Lumpkin, R., and K. Speer, 2007: Global ocean meridional overturning. *J. Phys. Oceanogr.*, **37**, 2550–2562, https://doi.org/10.1175/JPO3130.1.

Marshall, J., and K. Speer, 2012: Closure of the meridional overturning circulation through Southern Ocean upwelling. *Nat. Geosci.*, **5**, 171–180, https://doi.org/10.1038/ngeo1391.

Mashayek, A., R. Ferrari, M. Nikurashin, and W. R. Peltier, 2015: Influence of enhanced abyssal diapycnal mixing on stratification and the ocean overturning circulation. *J. Phys. Oceanogr.*, **45**, 2580–2597, https://doi.org/10.1175/JPO-D-15-0039.1.

——, H. Salehipour, D. Bouffard, C. P. Caulfield, R. Ferrari, M. Nikurashin, W. R. Peltier, and W. D. Smyth, 2017: Efficiency of turbulent mixing in the abyssal ocean circulation. *Geophys. Res. Lett.*, **44**, 6296–6306, https://doi.org/10.1002/2016GL072452.

McDougall, T. J., 1984: The relative roles of diapycnal and isopycnal mixing on subsurface water mass conversion. *J. Phys. Oceanogr.*, **14**, 1577–1589, https://doi.org/10.1175/1520-0485(1984)014<1577:TRRODA>2.0.CO;2.

——, 1989: Dianeutral advection. *Parameterization of Small-Scale Processes: Proc. 'Aha Huliko 'a Hawaiian Winter Workshop*, Honolulu, HI, University of Hawai'i at Mānoa, 289–315.

——, and R. Ferrari, 2017: Abyssal upwelling and downwelling driven by near-boundary mixing. *J. Phys. Oceanogr.*, **47**, 261–283, https://doi.org/10.1175/JPO-D-16-0082.1.

Melet, A., S. Legg, and R. Hallberg, 2016: Climatic impacts of parameterized local and remote tidal mixing. *J. Climate*, **29**, 3473–3500, https://doi.org/10.1175/JCLI-D-15-0153.1.

Munk, W. H., 1966: Abyssal recipes. *Deep-Sea Res. Oceanogr. Abstr.*, **13**, 707–730, https://doi.org/10.1016/0011-7471(66)90602-4.

Nikurashin, M., and R. Ferrari, 2011: Global energy conversion rate from geostrophic flows into internal lee waves in the deep ocean. *Geophys. Res. Lett.*, **38**, L08610, https://doi.org/10.1029/2011GL046576.

Oka, A., and Y. Niwa, 2013: Pacific deep circulation and ventilation controlled by tidal mixing away from the sea bottom. *Nat. Commun.*, **4**, 2419, https://doi.org/10.1038/ncomms3419.

Osborn, T. R., 1980: Estimates of the local rate of vertical diffusion from dissipation measurements. *J. Phys. Oceanogr.*, **10**, 83–89, https://doi.org/10.1175/1520-0485(1980)010<0083:EOTLRO>2.0.CO;2.

Phillips, O., 1970: On flows induced by diffusion in a stably stratified fluid. *Deep-Sea Res. Oceanogr. Abstr.*, **17**, 435–443, https://doi.org/10.1016/0011-7471(70)90058-6.

——, J.-H. Shyu, and H. Salmun, 1986: An experiment on boundary mixing: Mean circulation and transport rates. *J. Fluid Mech.*, **173**, 473–499, https://doi.org/10.1017/S0022112086001234.

Polzin, K. L., J. M. Toole, J. R. Ledwell, and R. W. Schmitt, 1997: Spatial variability of turbulent mixing in the abyssal ocean. *Science*, **276**, 93–96, https://doi.org/10.1126/science.276.5309.93.

Rhines, P., and P. MacCready, 1989: Boundary control over the large-scale circulation. *Parameterization of Small-Scale Processes: Proc. 'Aha Huliko 'a Hawaiian Winter Workshop*, Honolulu, HI, University of Hawai'i at Mānoa, 75–99.

Sheen, K. L., and Coauthors, 2014: Eddy-induced variability in Southern Ocean abyssal mixing on climatic timescales. *Nat. Geosci.*, **7**, 577–582, https://doi.org/10.1038/ngeo2200.

Smith, W. H., and D. T. Sandwell, 1997: Global sea floor topography from satellite altimetry and ship depth soundings. *Science*, **277**, 1956–1962, https://doi.org/10.1126/science.277.5334.1956.

St. Laurent, L. C., and C. Garrett, 2002: The role of internal tides in mixing the deep ocean. *J. Phys. Oceanogr.*, **32**, 2882–2899, https://doi.org/10.1175/1520-0485(2002)032<2882:TROITI>2.0.CO;2.

——, and A. M. Thurnherr, 2007: Intense mixing of lower thermocline water on the crest of the Mid-Atlantic Ridge. *Nature*, **448**, 680–683, https://doi.org/10.1038/nature06043.

——, J. Toole, and G. A. Schmidt, 2001: Buoyancy forcing by turbulence above rough topography in the abyssal Brazil Basin. *J. Phys. Oceanogr.*, **31**, 3476–3495, https://doi.org/10.1175/1520-0485(2001)031<3476:BFBTAR>2.0.CO;2.

——, H. L. Simmons, and S. R. Jayne, 2002: Estimating tidally driven mixing in the deep ocean. *Geophys. Res. Lett.*, **29**, 2106, https://doi.org/10.1029/2002GL015633.

——, A. C. Naveira Garabato, J. R. Ledwell, A. M. Thurnherr, J. M. Toole, and A. J. Watson, 2012: Turbulence and diapycnal mixing in Drake Passage. *J. Phys. Oceanogr.*, **42**, 2143–2152, https://doi.org/10.1175/JPO-D-12-027.1.

Stewart, K. D., G. O. Hughes, and R. W. Griffiths, 2012: The role of turbulent mixing in an overturning circulation maintained by surface buoyancy forcing. *J. Phys. Oceanogr.*, **42**, 1907–1922, https://doi.org/10.1175/JPO-D-11-0242.1.

Thompson, L., and G. C. Johnson, 1996: Abyssal currents generated by diffusion and geothermal heating over rises. *Deep-Sea Res. I*, **43**, 193–211, https://doi.org/10.1016/0967-0637(96)00095-7.

Thorpe, S. A., 1987: Current and temperature variability on the continental slope. *Philos. Trans. Roy. Soc. London*, **323A**, 471–517, https://doi.org/10.1098/rsta.1987.0100.

Toggweiler, J., and B. Samuels, 1995: Effect of Drake Passage on the global thermohaline circulation. *Deep-Sea Res. I*, **42**, 477–500, https://doi.org/10.1016/0967-0637(95)00012-U.

Toole, J. M., R. W. Schmitt, and K. L. Polzin, 1994: Estimates of diapycnal mixing in the abyssal ocean. *Science*, **264**, 1120–1123, https://doi.org/10.1126/science.264.5162.1120.

Umlauf, L., and H. Burchard, 2011: Diapycnal transport and mixing efficiency in stratified boundary layers near sloping topography. *J. Phys. Oceanogr.*, **41**, 329–345, https://doi.org/10.1175/2010JPO4438.1.

Visbeck, M., and M. Rhein, 2000: Is bottom boundary layer mixing slowly ventilating Greenland Sea deep water? *J. Phys. Oceanogr.*, **30**, 215–224, https://doi.org/10.1175/1520-0485(2000)030<0215:IBBLMS>2.0.CO;2.

Walin, G., 1982: On the relation between sea-surface heat flow and thermal circulation in the ocean. *Tellus*, **34**, 187–195, https://doi.org/10.3402/tellusa.v34i2.10801.

Waterhouse, A. F., and Coauthors, 2014: Global patterns of diapycnal mixing from measurements of the turbulent dissipation rate. *J. Phys. Oceanogr.*, **44**, 1854–1872, https://doi.org/10.1175/JPO-D-13-0104.1.

Watson, A. J., and A. C. Naveira Garabato, 2006: The role of Southern Ocean mixing and upwelling in glacial-interglacial atmospheric CO_2 change. *Tellus*, **58B**, 73–87, https://doi.org/10.1111/j.1600-0889.2005.00167.x.

Winters, K. B., P. Bouruet-Aubertot, and T. Gerkema, 2011: Critical reflection and abyssal trapping of near-inertial waves on a β-plane. *J. Fluid Mech.*, **684**, 111–136, https://doi.org/10.1017/jfm.2011.280.

Wunsch, C., 1970: On oceanic boundary mixing. *Deep-Sea Res. Oceanogr. Abstr.*, **17**, 293–301, https://doi.org/10.1016/0011-7471(70)90022-7.